(Received 19 September 2024, Accepted 7 January 2025, Scheduled 27 January 2025)

Low-frequency Excitation of a Stratified Conducting Sphere by Point Charges or Electric Dipoles

Mykola Bogomolov[1], Gregory B. Gajda[2], and Mykola Zhuk[2,*]

[1] *School of Mathematics, Statistics and Physics, Newcastle University, Herschel Building, Newcastle upon Tyne, NE1 7RU, UK*
[2] *Consumer and Clinical Radiation Protection Bureau, Health Canada*
775 Brookfield Road, A. L. 6302C, Ottawa, Ontario, K1A 1C1, Canada

ABSTRACT: This paper investigates the low-frequency excitation of a non-magnetic stratified conducting sphere by external sources, using a classical quasi-static approach. We focus on point-impressed sources represented by charges or electric dipoles, which predominantly generate electric fields. The findings have implications for low-frequency scattering theory and can potentially support the assessment of localized human exposure to low-frequency electric fields, such as those from Wireless Power Transfer using capacitive coupling technology.

For a sphere with an arbitrary number of homogeneous layers, we develop a numerical-analytical solution inspired by the Exact Difference Scheme. This approach yields a tridiagonal discretized representation of the continuous problem, ensuring uniqueness and computational stability, and allowing for efficient solution via the Thomas algorithm. For a sphere with general radial inhomogeneity, we apply the Finite Difference method. Computational experiments show a strong agreement between these two approaches.

We also examine the physical aspects of electric field interaction with a four-layer model of the human head, using the concept of coupling coefficients for the electric field and the generated heat. Our results show that these coupling coefficients increase with the separation between the point sources and the sphere, converging in certain cases to those for a uniform incident electric field. A comparison with the relevant ICNIRP reference levels for the incident electric field is also provided.

The comprehensive Wolfram Mathematica code, consisting of multiple modules and including theoretical definitions and explanations of the computed quantities, is available as a supplement to the paper.

1. INTRODUCTION

The motivation for this paper is twofold. First, it stems from the authors' interest in the low-frequency scattering theory for electromagnetic (EM) waves. Second, it addresses the need for a rational analysis of *localized* exposures of the human body to EM fields from Wireless Power Transfer (WPT).

The theory of low-frequency EM fields is based on the observation that the EM field and the impressed sources can be expanded in a series in powers of a *small parameter*, the angular frequency (ω) [51, 24, 2, 11, Ch. 3]. Consequently, theoretical analysis of the low-frequency excitation can be conducted using perturbation theory concepts and methods. This aligns with the fact that existing and prospective WPT technologies using near-field coupling operate at frequencies not exceeding a few hundred kHz [20].

In this context, the paper examines the low-frequency excitation of a conducting *sphere*. The inherent symmetries of this problem allow for efficient analysis, revealing fundamental features of EM-object interaction that are broadly applicable to other objects. The sphere thus serves as an excellent reference case for analyzing properties, validating numerical simulation techniques, and generating calibration data for measurements. For these reasons, the model involving a conducting spherical object is of significant interest across many applications. We illustrate the physical and practical relevance of spherical models by considering several examples pertinent to the low-frequency range.

In exploration geophysics, the quasi-static solution for the excitation of a stratified conducting sphere by an incident magnetic field is fundamental to magnetotelluric methods [64, 4, Ch. 4], while excitation by an electric dipole is key to wireless EM methods [15]. Both approaches are used to remotely probe the Earth's internal structure. Similarly, the homogeneous or two-layer conducting sphere, representing an underground object such as an ore body in a conductive medium, is relevant to electrical resistivity and induced polarization methods for near-surface sounding [54, pp. 60–79, 62, Chs. I, II]. (It is worth clarifying that in this Section, "stratified" refers to a penetrable spherical body composed of concentric layers, each homogeneous, with the number of layers being a variable model parameter, as opposed to fixed-layer models.)

In EM materials engineering, electrically small spheres serve as structural elements [46, 47, 29]. The low-frequency excitation of a stratified conducting sphere by embedded electric dipoles serves as a canonical model for the human head in electroencephalography (EEG) and magnetoencephalography (MEG). In EEG, the quasi-static solution for the induced electric field is of interest, while in MEG, the focus is on the quasi-static solution for the induced magnetic field [35, Ch. 6, 10].

* Corresponding author: Mykola Zhuk (mykola.zhuk@hc-sc.gc.ca).

Finally, spherical models are widely used in analytical and numerical dosimetry to study EM field interactions with the human body and its parts [12, 28, 50].

We begin our review of relevant prior research with *exact* solutions that are valid at any frequency. These solutions can be applied directly to the low-frequency range, serve as sources for low-frequency approximations, and act as benchmark solutions for validating the latter.

For plane-wave scattering by a penetrable sphere, the literature is extensive. The Mie solution for a homogeneous sphere is well-covered in [18, Ch. 9], and its generalizations, including to a stratified sphere, are summarized in [57, Sec. 11.3, 65], and [36, Ch. 7].

When sources are confined to a *finite* point in space, EM field quantities can be derived from the corresponding sources (point dipoles) or using dyadic Green's functions (GFs) [55, 57, Sec. 1.6]. In the review below, any mention of dipolar excitation implies that the corresponding analyses apply to arbitrarily oriented dipoles or can be easily generalized to such cases.

Explicit solutions for a homogeneous conducting sphere in a conducting medium irradiated by an external magnetic or electric dipole are provided in [30] and [59], respectively. For radially inhomogeneous dielectric media with continuous permittivity profiles, explicit solutions for the electric dyadic GF are given in [66]. (Note a minor error in [66]: the solutions to Eqs. (14) and (15) for the radial functions corresponding to superscript $p = 1$ should be selected based on the requirement that they vanish as the radial variable approaches zero, rather than by imposing a standing wave condition at infinity.)

The EM field due to an arbitrarily oriented electric dipole in or around a homogeneous spherical particle is explored in [6, 8], while the electric field due to an electric dipole inside or outside a stratified sphere is treated in [7]. The four dyadic GFs for electric and magnetic dipoles in a stratified medium are constructed in [27], and the electric and magnetic dyadic GFs for an electric dipole outside a stratified sphere are provided in [42], although no numerical implementation details are reported in these works. The T-matrix method is used in [40] to derive the electric dyadic GF for a single electric dipole located inside or outside a stratified sphere, potentially with a perfect electric conductor (PEC) core, with numerical examples provided. The same spherical model is extended in [23] to consider the case of multiple arbitrarily located electric dipoles. An analysis of the EM field due to an external electric dipole irradiating a stratified conducting sphere in a conductive medium is detailed in [62, Appendix A]. A robust transfer-matrix solution for an electric dipole radiating inside and outside a stratified sphere is developed in [31] and validated numerically, with accompanying computer code provided in [41].

The exact dipole excitation solutions for penetrable spheres in [30, 59, 40, 23] have been adapted for the low-frequency range, yielding low-frequency approximations for the scattered EM field in both the near zone [30, 59] and far zone [40, 23]. In [40] and [23], these approximations have also been applied in the analysis of related inverse scattering problems.

Our review of works using *low-frequency* approximations focuses on spherical objects that are either PECs or have finite nonzero conductivity, and are excited by point-like sources.

Higher-order terms in the low-frequency expansions for a PEC sphere excited by an external magnetic dipole are derived in [58] and [52] for conducting and lossless ambient media, respectively. Quasi-static solutions for a penetrable sphere in free space consisting of two conducting layers or three layers (a conducting core, a conducting outer shell, and a free-space layer between them) are presented in [60] and [61], respectively, for an external magnetic monopole excitation. The EM field due to electric or magnetic multipole excitation can be obtained by differentiating the solution for an electric or magnetic monopole with respect to source coordinates, as highlighted in [61] and employed in this paper.

Quasi-static solutions and numerical analyses for the electric potential produced by an electric dipole inside a four-layer isotropic conducting sphere in non-conductive space are reported in [37] and [33], with the latter validating the analytical model against Finite Element Method simulations. For stratified anisotropic conducting spheres, the quasi-static electric and magnetic fields due to an internal electric dipole are derived and validated in [39] and [34]. Anisotropy here refers to differing radial and tangential conductivities within each layer. These solutions build on the general analytical results for potential distributions in stratified spheres with anisotropic conductivity due to internal electric monopoles, derived in [32], which also addresses spheroidal inhomogeneous anisotropic media.

In this paper, we focus on non-magnetic isotropic *radially inhomogeneous* conducting spheres composed of an *arbitrary* number of concentric continuous layers, within the low-frequency framework. The problem formulations follow the approach outlined in [51]. We examine the excitation of these spheres by external *point* impressed sources, such as charges or electric dipoles. Point sources like these are fundamental for modeling arbitrary spatial source distributions [57, Sec. 3.3]. At low frequencies, they primarily generate *electric* fields [14, Sec. 6.5]. Our emphasis on electric fields aligns with emerging WPT technologies [9, 13, 63], which rely on capacitive coupling and predominantly produce electric fields. The results are implemented in a Wolfram Mathematica code, provided as a supplement.

Initially, we concentrate on the sphere with *homogeneous* layers, which has applications in its own right and can also serve as an approximation to an inhomogeneous sphere with arbitrary radial conductivity dependence by replacing it with multiple sufficiently thin homogeneous layers — refer to, e.g., [22, 38], for similar treatments of analogous EM scattering problems. In Section 2, we combine *analytical* derivations with *numerical* techniques to efficiently compute the induced electric field within a piecewise-homogeneous sphere with an arbitrary number of layers and positions of impressed sources outside the sphere. Inspired by the Exact Difference Scheme (EDS) introduced in [56] and [16], our approach leverages its perfect suitability for this context. Notably, it yields a *tridiagonal* discretized equivalent of the continuous problem, ensuring *uniqueness* and computational *stability*. Moreover, it facil-

itates numerical solution through a left elimination version of the *Thomas algorithm* [44, § 1.1, pp. 9–10], [1, § 2–3, pp. 52–54]. The program implementation of this numerical-analytical approach is presented in Modules 1 to 8 of the code supplement.

In Section 3, we examine the sphere with *general* radial inhomogeneity. To analyze the excitation of such a sphere, we used a *direct* numerical approach based on the finite difference (FD) method [44, 26]. This not only provided an independent tool to validate the EDS-based solution, but also produced a robust computational tool for efficient analysis of practical exposure problems. The FD code is detailed in Modules 9 to 18 of the supplement.

In Section 4, we demonstrate the effectiveness of the numerical-analytical and FD solutions by examining a *four-layer* sphere model that simulates the human head at low frequencies [35, Ch. 6, 33, 37]. Our computational experiments show a strong agreement between the two solutions. To explore the physical aspects of the electric field interaction with this model, we analyzed the coupling coefficients for the electric field (K_E) and the generated heat (K_Q) for various impressed sources, including point charges, linearly or circularly polarized dipoles, and uniform incident fields generated by infinitely remote sources. Implementation details are provided in Modules 19A to 29 of the code supplement.

The FD solution proved to be particularly efficient, allowing for analysis of various scenarios through simple search across the FD grid nodes. Our findings include that a) the coupling coefficients for the uniform incident field *exceed* those for localized sources; b) the coupling coefficients for point sources *increase* with the distance between the sphere and the sources; c) for a point charge, a linearly polarized dipole aligned with one of the Cartesian axes, or a circularly polarized dipole with a horizontal (x-y) plane of polarization, the coupling coefficients *converge* to those for the uniform incident field; and d) the maximum magnitude of the induced electric field and the maximum generated heat are achieved at the *structural interfaces* of the radially inhomogeneous medium, rather than within its continuous regions.

Throughout the paper, the symbol i denotes the imaginary unit, and the time convention $e^{-i\omega t}$ is used for time-harmonic sources and fields. This work was completed using Wolfram Mathematica 12 from Wolfram Research (Champaign, IL).

2. NUMERICAL-ANALYTICAL SOLUTION

2.1. Model Setup

Let us consider a conducting body $\mathcal{B}$ in the form of *sphere* with radius a, centered at the origin of a Cartesian coordinate system x, y, z, and embedded in free space $\mathcal{F}$ with absolute permittivity ε_0 and permeability μ_0. The body is *non-magnetic*, meaning permeability equals that of vacuum (μ_0). In the low-frequency approximation, the only material property that determines the induced electric field $\mathbf{E}$ is the body's conductivity k. We focus on the *spherically stratified* body where the conductivity k varies radially, $k = k(r)$. A graphical illustration of the stratified sphere is shown in Fig. 1.

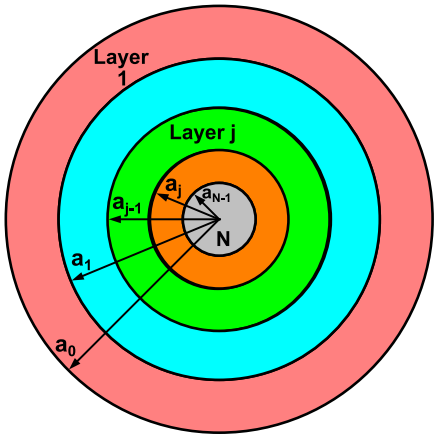

FIGURE 1. N-layer sphere.

In this model, the body $\mathcal{B}$ consists of N concentric spherical layers, numbered sequentially from the outermost layer ($j = 1$) to the innermost layer ($j = N$). The outer boundary at $r = a$ is denoted by $\mathcal{S}$. The interface between the jth and $(j+1)$th layers (referred to as "interface j") is a spherical surface with radius a_j and is centered at the origin. The function $k(r)$ is assumed to be smooth and positive within each layer, but may have a jump discontinuity at an interface.

For notational consistency, the radius of the sphere is also denoted as a_0, so that the symbol a_0 in Fig. 1 is the same as a. Sometimes, we use the convention that $a_N = 0$. Note that the largest radius (a_0) has the lowest index.

Anticipating further needs, it is convenient to introduce the spherical coordinates r, θ, ϕ, having directed the polar axis along the z axis (Fig. 2):

$$x = r\sin\theta\cos\phi, \quad y = r\sin\theta\sin\phi, \quad z = r\cos\theta \quad (1)$$
$$(0 \le r < +\infty, \quad 0 \le \theta \le \pi, \quad 0 \le \phi < 2\pi)$$

(θ is the angle from the z axis, and ϕ is the azimuthal angle). For simplicity, if the coordinates x, y, z are given in terms of r, θ, ϕ according to Eq. (1), we will use the same notation for a function of a point in space, regardless of how the point is represented in different coordinate systems. For example, $\mathbf{E}_b(\mathbf{r})$ and $\mathbf{E}_b(r, \theta, \phi)$ both denote the same function of a point in space.

The body is excited by impressed charges with a volume density distribution $\rho(\mathbf{r})$, which are assumed to be located outside the body. In the low-frequency approximation, the resulting

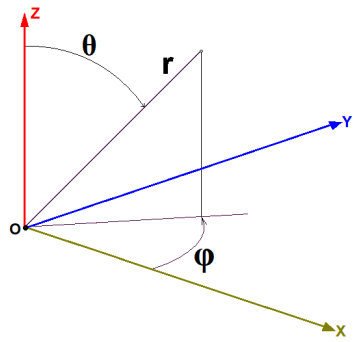

FIGURE 2. Spherical coordinates r, θ, ϕ.

electric field is potential, and its complex amplitude $\mathbf{E}(\mathbf{r})$ can be represented as the gradient of a scalar function:

$$\mathbf{E}(\mathbf{r}) = -\nabla V(\mathbf{r}), \tag{2}$$

where the minus sign is conventional but not critical to the analysis. To indicate whether a quantity refers to free space ($\mathcal{F}$) or the body ($\mathcal{B}$), we will use the subscripts 0 and b, respectively.

The problem for V_0 [51] is completely separated from the problem for V_b. The former is equivalent to the problem described in [53, Ch. III, 48, Ch. I, 57, Ch. 4], which addresses the potential generated by an impressed charge distribution outside body $\mathcal{B}$ as if it were an insulated PEC with no net charge on its surface S.

The problem for V_b is solved *after* obtaining the solution V_0 in free space, as the latter is used in the boundary condition for V_b on S through the quantity

$$\sigma(\theta,\phi) = -\,\varepsilon_0 \frac{\partial V_0}{\partial r}\bigg|_{r=a}. \tag{3}$$

If $\mathcal{B}$ were a PEC, this value of $\sigma(\theta,\phi)$ would represent the surface charge density on the PEC surface S.

If the quantity $\sigma(\theta,\phi)$ is known, the potential inside the body can be derived by solving the following BVP, which admits a unique solution:

$$\left[\frac{1}{r^2}\frac{\partial}{\partial r} r^2 k(r) \frac{\partial}{\partial r} + \frac{k(r)}{r^2}\Delta_\Omega\right] V_b(r,\theta,\phi) = 0, \tag{4}$$

$$k(r)\frac{\partial V_b(r,\theta,\phi)}{\partial r} = i\omega\sigma(\theta,\phi), \quad (r=a) \tag{5}$$

$$\{V_b(r,\theta,\phi)\} = 0, \quad \left\{k(r)\frac{\partial V_b(r,\theta,\phi)}{\partial r}\right\} = 0 \tag{6}$$

$$V_b(r,\theta,\phi) = 0 \quad (r=0) \tag{7}$$

Here, Δ_Ω is the spherical Laplacian:

$$\Delta_\Omega = \frac{1}{\sin\theta}\frac{\partial}{\partial\theta}\sin\theta\frac{\partial}{\partial\theta} + \frac{1}{\sin^2\theta}\frac{\partial^2}{\partial\varphi^2}. \tag{8}$$

The partial differential equation (PDE) (4) is applied to all points in each layer $j = 1, 2, \ldots, N$ of the medium, except the origin ($r = 0$), where the Laplacian in spherical coordinates has a singular point. Eq. (5) is the boundary condition on the outer boundary of the sphere. Eq. (6) defines the conditions at each interface $r = a_j$ ($j = 1, 2, \ldots, N-1$) between the layers. The curly braces denote the jump of the bracketed quantity across an interface. The condition at the origin, given by Eq. (7), encompasses the boundedness of the solution at $r = 0$ and also ensures the uniqueness[1] of the solution by setting the potential to zero at the origin.

The above problem for V_b is a Neumann BVP because the normal derivative of V_b is specified on the outer boundary S of the domain. As is well known [49, p. 512, Prob. 8.3.6], the Neumann problem (4)–(7) has a solution only if the boundary data σ satisfies the solvability condition:

$$\int_S \sigma(\theta,\phi)dS = 0. \tag{9}$$

In our case, Eq. (9) is automatically satisfied because it is part of the problem formulation for V_0.

From here, we describe vector quantities in terms of their Cartesian coordinates (with subscripts x, y, z), and also in terms of spherical coordinates using local basis vectors $\mathbf{e}_1(\theta,\phi), \mathbf{e}_2(\theta,\phi), \mathbf{e}_3(\phi)$ along the directions of increasing r, θ, and ϕ, respectively:

$$\mathbf{e}_1(\theta,\phi) = \mathbf{x}_0\sin\theta\cos\phi + \mathbf{y}_0\sin\theta\sin\phi + \mathbf{z}_0\cos\theta, \tag{10}$$

$$\mathbf{e}_2(\theta,\phi) = \mathbf{x}_0\cos\theta\cos\phi + \mathbf{y}_0\cos\theta\sin\phi - \mathbf{z}_0\sin\theta, \tag{11}$$

$$\mathbf{e}_3(\phi) = -\mathbf{x}_0\sin\phi + \mathbf{y}_0\cos\phi. \tag{12}$$

Here, $\mathbf{x}_0, \mathbf{y}_0, \mathbf{x}_0$ are the unit vectors for the Cartesian coordinate system. The spherical coordinates of a vector will be labeled with subscripts 1, 2, and 3. The spherical coordinates r, θ, ϕ of the observation point $\mathbf{r}$ are indicated as arguments of the local basis vectors only where necessary for clarity. For example, $\mathbf{e}_1$ denotes $\mathbf{e}_1(\theta,\phi)$, etc. Using this notation, the electric field vector $\mathbf{E}_b$ inside the sphere is given by:

$$\mathbf{E}_b(\mathbf{r}) = \mathbf{e}_1 E_{b1}(r,\theta,\phi) + \mathbf{e}_2 E_{b2}(r,\theta,\phi) + \mathbf{e}_3 E_{b3}(r,\theta,\phi). \tag{13}$$

2.2. Excitation by a Point Charge

Scalar potential. In the special case of a point charge q located near the sphere at position $\mathbf{r}'$ ($r' > a$), the charge density is given by:

$$\rho(\mathbf{r}) = q\delta(\mathbf{r} - \mathbf{r}'), \tag{14}$$

where δ is the Dirac delta function. The location of $\mathbf{r}'$ is arbitrary; the source point need not be on any of the coordinate axes x, y or z. The corresponding potential V_0 outside the sphere ($r > a$) is obtained using the method of images [21, p. 61, Eq. (2.8)]:

$$V_0(\mathbf{r}) = V^{(inc)}(\mathbf{r}) + \frac{1}{4\pi\varepsilon_0}\left(\frac{q_*}{|\mathbf{r} - \mathbf{r}_*|} + \frac{q_{**}}{r}\right), \tag{15}$$

where

$$V^{(inc)}(\mathbf{r}) = \frac{1}{4\pi\varepsilon_0}\frac{q}{|\mathbf{r} - \mathbf{r}'|} \tag{16}$$

is the incident potential generated by the point charge in free space without the sphere. The point $\mathbf{r}_*$ and charge q_* are defined as:

$$\mathbf{r}_* = \frac{a^2}{r'^2}\mathbf{r}', \tag{17}$$

$$q_* = -q\frac{a}{r'}, \tag{18}$$

with $q_{**} = -q_*$. We observe that the image sources of this field comprise a charge q_* at point $\mathbf{r}_*$ inside the sphere and a charge $q_{**} = -q_*$ at the origin [21, Sec. 2.3, p. 61].

[1] Replacing the zero on the right side of Eq. (7) with an arbitrary constant would yield a solution differing by that constant, but the induced electric field derived from (2) would remain unchanged, regardless of the constant's value.

Substitute in Eq. (15) the expansion [21, p. 102, Eq. (3.38)]

$$\frac{1}{|\mathbf{r}-\mathbf{r}'|}=\sum_{l=0}^{+\infty}\frac{r_<^l}{r_>^{l+1}}P_l(\cos\gamma), \tag{19}$$

and the corresponding expression

$$\frac{1}{|\mathbf{r}-\mathbf{r}_*|}=\frac{1}{r}\sum_{l=0}^{+\infty}\frac{a^{2l}}{(rr')^l}P_l(\cos\gamma), \tag{20}$$

where $r_<$ and $r_>$ are the smaller and larger of r and r', and $P_l(\alpha)$ is the Legendre polynomial of order l in α [21, p. 98, Eq. (3.16)]:

$$P_l(\alpha)=\frac{1}{2^l l!}\frac{d^l}{d\alpha^l}(\alpha^2-1)^l. \tag{21}$$

Here γ ($0\le\gamma\le\pi$) is the angle between the vectors $\mathbf{r}$ and $\mathbf{r}'$:

$$\cos\gamma=\mathbf{e}_1\cdot\mathbf{e}_1'=\cos\theta\cos\theta'+\sin\theta\sin\theta'\cos(\phi-\phi'). \tag{22}$$

Primed quantities are associated with the source point $\mathbf{r}'$, such as $\mathbf{e}_1'=\mathbf{e}_1(\theta',\phi')$, etc. (To be clear, ordinarily the prime is used to represent a derivative, but in this paper derivatives are never denoted by primes.)

Considering the expression derived from Eq. (3), we can represent the quantity σ as (cf. [53, Sec. 3.22, p. 203, Eq. (8)])

$$\sigma(\theta,\phi)=-\frac{q}{4\pi}\sum_{l=1}^{+\infty}(2l+1)\frac{a^{l-1}}{r'^{l+1}}P_l(\cos\gamma). \tag{23}$$

Based on this representation, we seek V_b in the following form:

$$V_b(r,\theta,\phi)=-\frac{i\omega q}{4\pi}\sum_{l=1}^{+\infty}(2l+1)\frac{a^{l-1}}{r'^{l+1}}P_l(\cos\gamma)v(r|l), \tag{24}$$

where the expansion coefficients $v(r|l)$ are yet to be determined. Substituting expansion (24) in Eqs. (4)–(7), taking into consideration that [21, p. 110, Eq. (3.64)]

$$\Delta_\Omega P_l(\cos\gamma)+l(l+1)P_l(\cos\gamma)=0, \tag{25}$$

and using expression (23), we obtain that for each value of the parameter $l=1,2,\ldots$ the function $v(r|l)$ satisfies the ordinary differential equation (ODE)

$$\frac{d}{dr}r^2k(r)\frac{dv(r|l)}{dr}-l(l+1)k(r)v(r|l)=0 \tag{26}$$

when r is confined to an interval corresponding to a layer ($j=1,2,\ldots,N$), as well as the boundary condition

$$k(r)\frac{dv(r|l)}{dr}=1\quad(r=a) \tag{27}$$

the conjunction conditions

$$\{v(r|l)\}=0,\quad\left\{k(r)\frac{dv(r|l)}{dr}\right\}=0 \tag{28}$$

at the points $r=a_j$ ($j=1,2,\ldots,N-1$), and the requirement

$$|v(r|l)|<\infty\quad(r\to 0) \tag{29}$$

at the singular point $r=0$.

We have thus reduced the three-dimensional BVP (4)–(7) to a one-dimensional problem for the functions $v(r|l)$ ($l=1,2,3,\ldots$). These functions form the key building blocks of our numerical-analytical approach. We will revisit these functions, examine some of their properties, and present an efficient algorithm for their computation later in this section, specifically for a *piecewise-homogeneous* sphere.

Electric field. A useful relation is introduced next, namely

$$\nabla\cos\gamma=\frac{1}{r}\left(\mathbf{e}_2\,\mathbf{e}_2\cdot\mathbf{e}_1'+\mathbf{e}_3\,\mathbf{e}_3\cdot\mathbf{e}_1'\right). \tag{30}$$

To derive this expression, we used the formulas

$$\frac{\partial\cos\gamma}{\partial\theta}=\mathbf{e}_2\cdot\mathbf{e}_1',\quad\frac{\partial\cos\gamma}{\partial\phi}=\sin\theta\mathbf{e}_3\cdot\mathbf{e}_1', \tag{31}$$

which follow from Eq. (22) by differentiation with respect to θ and ϕ and taking into account that

$$\frac{\partial\mathbf{e}_1}{\partial\theta}=\mathbf{e}_2,\quad\frac{\partial\mathbf{e}_1}{\partial\phi}=\sin\theta\mathbf{e}_3. \tag{32}$$

Based on Eqs. (2) and (24) and using Eq. (30), we can derive the following expressions for the spherical coordinates of the induced electric field vector:

$$E_{b1}(r,\theta,\phi)=\frac{i\omega q}{4\pi r'^2}A(r,\theta,\phi), \tag{33}$$

$$E_{bm}(r,\theta,\phi)=\frac{i\omega q}{4\pi r'^2}\mathbf{e}_m\cdot\mathbf{e}_1'B(r,\theta,\phi)\quad(m=2,3) \tag{34}$$

where

$$A(r,\theta,\phi)=\sum_{l=1}^{+\infty}(2l+1)\left(\frac{a}{r'}\right)^{l-1}P_l(\cos\gamma)\dot{v}(r|l), \tag{35}$$

$$B(r,\theta,\phi)=\frac{1}{r}\sum_{l=1}^{+\infty}(2l+1)\left(\frac{a}{r'}\right)^{l-1}\dot{P}_l(\cos\gamma)v(r|l). \tag{36}$$

In these expressions, a dot $\cdot$ appearing above a function indicates ordinary differentiation with respect to the argument:

$$\dot{v}(r|l)=\frac{dv(r|l)}{dr},\quad\dot{P}_l(\alpha)=\frac{dP_l(\alpha)}{d\alpha}, \tag{37}$$

etc. We are using this symbol in order to avoid confusion since prime notation which is usually reserved for derivatives is associated in this paper with the source point $\mathbf{r}'$.

2.3. Excitation by a Point Dipole

Dipole at arbitrary location. The other charge distribution that we consider is:

$$\rho(\mathbf{r}) = \mathbf{p} \cdot \nabla' \delta(\mathbf{r} - \mathbf{r}') \tag{38}$$

where ∇' is the nabla operator acting on the primed variable $\mathbf{r}'$, and:

$$\mathbf{p} = \mathbf{x}_0 p_x + \mathbf{y}_0 p_y + \mathbf{z}_0 p_z. \tag{39}$$

Here, p_x, p_y, p_z are arbitrary complex *constants* with respect to the variable $\mathbf{r}$. This charge distribution represents a point dipole with an electric moment $\mathbf{p}$ [57, Eq. (3.30)].

The potential V_b due to a point dipole is derived by applying the operator $\mathbf{p} \cdot \nabla'$ to the potential (24) for a point charge with $q = 1$. The resulting expression is as follows:

$$V_b(r,\theta,\phi) = \frac{i\omega}{4\pi} \sum_{l=1}^{+\infty} (2l+1) \frac{a^{l-1}}{r'^{l+2}} v(r|l)$$

$$\rightarrow \left[p'_1 (l+1) P_l(\cos\gamma) - (\mathbf{e}_1 \cdot \mathbf{p}'_\perp) \dot{P}_l(\cos\gamma) \right]. \tag{40}$$

Here, the quantities used are:

$$p'_1 = \mathbf{p} \cdot \mathbf{e}'_1, \tag{41}$$

$$\mathbf{p}'_\perp = \mathbf{p} - \mathbf{e}'_1 p'_1. \tag{42}$$

They characterize the electric dipole moment $\mathbf{p}$ in terms of the *local* basis $\mathbf{e}'_1$, $\mathbf{e}'_2$, $\mathbf{e}'_3$ at the source point $\mathbf{r}'$. This passage also uses a formula $\nabla' \cos\gamma$, obtained from Eq. (30) by interchanging the primed and unprimed quantities.

Regarding the electric field vector $\mathbf{E}_b$ within the sphere, we compute it by taking the negative gradient of the potential, as indicated in Eq. (2). Using the representation from (40), we get the following expressions: for the radial component —

$$E_{b1}(r,\theta,\phi) = \frac{i\omega}{4\pi} \sum_{l=1}^{+\infty} (2l+1) \frac{a^{l-1}}{r'^{l+2}} \dot{v}(r|l)$$

$$\rightarrow \left[\mathbf{e}_1 \cdot \mathbf{p}'_\perp \dot{P}_l(\cos\gamma) - p'_1 (l+1) P_l(\cos\gamma) \right], \tag{43}$$

and for the transverse component ($m = 2, 3$) —

$$E_{bm}(r,\theta,\phi) = \frac{i\omega}{4\pi r} \cdot \sum_{l=1}^{+\infty} (2l+1) \frac{a^{l-1}}{r'^{l+2}} v(r|l)$$

$$\rightarrow \left[(\mathbf{e}_m \cdot \mathbf{e}'_1) \left(\ddot{P}_l(\cos\gamma) (\mathbf{e}_1 \cdot \mathbf{p}'_\perp) - p'_1 (l+1) \dot{P}_l(\cos\gamma) \right) \right.$$

$$\left. + (\mathbf{e}_m \cdot \mathbf{p}'_\perp) \dot{P}_l(\cos\gamma) \right]. \tag{44}$$

To derive these representations, we used the expression for $\nabla(\mathbf{e}_1 \cdot \mathbf{p}'_\perp)$:

$$\nabla(\mathbf{e}_1 \cdot \mathbf{p}'_\perp) = \frac{1}{r} \left(\mathbf{e}_2 \mathbf{e}_2 \cdot \mathbf{p}'_\perp + \mathbf{e}_3 \mathbf{e}_3 \cdot \mathbf{p}'_\perp \right). \tag{45}$$

This equation can be easily verified using the formulas from Eq. (32).

Note that the quantities $\{v(r|l)\}_{l=1}^{\infty}$ in Eqs. (40) and (43)–(44) are the *same* as those used in Eqs. (24) and (33)–(34) for a point charge.

Dipole on the z axis. When the point dipole is positioned in free space on the positive z axis at a distance h from the sphere's surface, the source point is given by:

$$\mathbf{r}' = \mathbf{z}_0 z', \quad z' = a + h. \tag{46}$$

In this setup, the quantity $\cos\gamma$ from Eq. (22) is equal to $\cos\theta$. The quantities p'_1 and $\mathbf{p}'_\perp$ from Eqs. (41)–(42) are:

$$p'_1 = p_z, \tag{47}$$

$$\mathbf{p}'_\perp = \mathbf{x}_0 p_x + \mathbf{y}_0 p_y, \tag{48}$$

resulting in

$$\mathbf{e}_1 \cdot \mathbf{p}'_\perp = (p_x \cos\phi + p_y \sin\phi) \sin\theta. \tag{49}$$

Consequently, the scalar potential V_b from Eq. (40) can be expressed as

$$V_b(r,\theta,\phi) = i\omega (p_x \cos\phi + p_y \sin\phi) W_\perp(r,\theta) + i\omega p_z W_\parallel(r,\theta). \tag{50}$$

The functions $W_\perp$ and $W_\parallel$, which notably do not depend on the variable ϕ, are given by the following expressions:

$$W_\perp(r,\theta) = -\frac{\sin\theta}{4\pi} \sum_{l=1}^{+\infty} (2l+1) \frac{a^{l-1}}{r'^{l+2}} \dot{P}_l(\cos\theta) v(r|l), \tag{51}$$

$$W_\parallel(r,\theta) = \frac{1}{4\pi} \sum_{l=1}^{+\infty} (2l+1)(l+1) \frac{a^{l-1}}{r'^{l+2}} P_l(\cos\theta) v(r|l). \tag{52}$$

The corresponding expressions for the induced electric field can be easily derived from Eqs. (2) and (50). We omit these derivations for brevity.

2.4. Exact Difference Scheme (EDS)

The problem of finding the functions $\{v(r|l)\}_{l=1}^{\infty}$ can be solved exactly when the conductivity function $k(r)$ is constant within each layer ($j = 1, 2, \ldots, N$):

$$k(r) = k_j = \text{const}_j \quad (k_j > 0) \tag{53}$$

It is not assumed that the conductivities of adjacent layers are necessarily different; in other words, it is possible that $k_j = k_{j+1}$ for layers j and $j+1$.

This model has its own applications [35, Ch. 6] and can be used to approximate an inhomogeneous sphere with an arbitrary functional form for $k(r)$ by replacing it with multiple sufficiently thin homogeneous layers — see, for example, [22, 38] for a similar treatment of analogous EM scattering problems.

We derive the solution using a recurrence algorithm originally developed in [43] for the EDS designed for differential equations with discontinuous coefficients (for the latest developments in this approach, see [16]). In [43, 16] the solutions are defined for the overlapping *pairs* of consecutive layers. This requires solving Eq. (26) for each layer in the pair and then matching the solutions at the interface between the two layers.

We made a slight modification to that algorithm to simplify its application. Specifically, we solve Eq. (26) locally for *each*

layer, and then patch the solutions together at the interfaces according to the interface conditions (28).

Stencil functions. For a fixed l, consider the ordinary differential equation (ODE):

$$\frac{d}{dr}r^2\frac{du(r)}{dr} - l(l+1)u(r) = 0 \qquad (54)$$
$$(a_j < r < a_{j-1})$$

defined on the interval corresponding to the jth layer ($j = 1, 2, \ldots, N$). This ODE follows from Eq. (26) for the case of a homogeneous layer. As a reminder, in our notation, a_0 and a refer to the same value — the radius of the sphere, and we set $a_N = 0$, as previously mentioned.

It is worth mentioning that the term with $l = 0$ is absent in series (24), suggesting that it could be omitted from the analysis. However, to maintain generality, we assume $l = 0, 1, 2, \ldots$ until further notice.

For each shell layer ($j = 1, 2, \ldots, N-1$), we introduce the solutions $L_j(r|l), R_j(r|l) = u(r)$ for Eq. (54), defined by the following boundary conditions:

$$L_j(a_j|l) = 1, \quad L_j(a_{j-1}|l) = 0, \qquad (55)$$
$$R_j(a_j|l) = 0, \quad R_j(a_{j-1}|l) = 1. \qquad (56)$$

These *stencil* functions[2] are linearly independent and can be represented as follows:

$$L_j(r|l) = \frac{(a_j/a_{j-1})^{l+1}}{1-(a_j/a_{j-1})^{2l+1}}\left[\left(\frac{a_{j-1}}{r}\right)^{l+1} - \left(\frac{r}{a_{j-1}}\right)^{l}\right], \qquad (57)$$

$$R_j(r|l) = \frac{(a_j/a_{j-1})^{l}}{1-(a_j/a_{j-1})^{2l+1}}\left[\left(\frac{r}{a_j}\right)^{l} - \left(\frac{a_j}{r}\right)^{l+1}\right] \qquad (58)$$
$$(a_j < r < a_{j-1})$$

For the core ($j = N$), we use the stencil function $u(r) = R_N(r|l)$ determined by the boundary conditions

$$|R_N(0|l)| < \infty \quad (r \to 0) \qquad (59)$$
$$R_N(a_{N-1}|l) = 1. \qquad (60)$$

It is straightforward to verify that:

$$R_N(r|l) = \left(\frac{r}{a_{N-1}}\right)^{l} \quad (0 < r < a_{N-1}) \qquad (61)$$

In our context, $R_N(0|0)$ is defined as 1. Within the interval ($a_j \le r \le a_{j-1}$), the stencil functions (57), (58) and (61) have their values in the range $[0, 1]$. Moreover, for $l = 1, 2, 3, \ldots$, the stencil functions $L_j(r|l)$ are strictly decreasing, while $R_j(r|l)$ are strictly increasing because $dL_j(r|l)/dr < 0$ and $dR_j(r|l)/dr > 0$.

Discretization of the problem. To proceed, we introduce the (as yet unknown) values $v_j(l)$ of the function $v(r|l)$ at the N points a_j, where:

$$0 < a_{N-1} < a_{N-2} < \ldots < a_1 < a_0, \qquad (62)$$

[2] The letters L and R in L_j, R_j ($j = 1, 2, \ldots, N-1$) refer to the fact that the solution to Eq. (54) on an interval $a_j < r < a_{j-1}$ that assumes prescribed values $u(a_j)$, $u(a_{j-1})$ at the *left* and *right* endpoints, respectively, can be expressed as $u(r) = u(a_j)L_j(r|l) + u(a_{j-1})R_j(r|l)$.

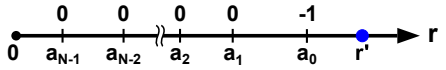

FIGURE 3. Nodes on sphere's surface and the interfaces for a point charge outside the sphere. The numbers positioned above the horizontal axis denote the forcing terms present on the right-hand side of Eqs. (66), (69), and (73).

i.e., on the sphere's surface and the interfaces:

$$v_j(l) = v(a_j|l) \quad (j = 0, 1, \ldots, N-1) \qquad (63)$$

As mentioned earlier, the problem we are addressing, namely that of a point source outside a conducting sphere, restricts the use of l to positive integer values. Consequently, we will only consider $l \ge 1$ from this point onward. Also note that the nodes (62) are numbered from *right to left,* i.e.,the largest node (a_0) has the lowest index.

In Fig. 3, the locations of the nodes defined by Eq. (62) are illustrated. The numbers (0 and -1) above the horizontal axis represent the forcing terms on the right-hand side parts of subsequent Eqs. (66), (69), and (73).

It can be easily verified by direct substitution that for the conductivity (53) the expressions within the shell layers ($j = 1, 2, 3, \ldots, N-1$)

$$v(r|l) = v_j(l)L_j(r|l) + v_{j-1}(l)R_(r|l) \quad (a_j \le r \le a_{j-1}) \qquad (64)$$

and the core (layer N)

$$v(r|l) = v_{N-1}(l)R_N(r|l) \quad (0 \le r < a_{N-1}) \qquad (65)$$

satisfy the ODE (26), the first of the interface conditions (28) and the requirement at the origin (29) for any values of the N unknowns $\{v_j(l)\}_{j=0}^{N-1}$.

After imposing boundary condition (27) on representation (64) specialized to the first layer ($j = 1$) we obtain the relation

$$-C_0(l)v_0(l) + B_0(l)v_1(l) = -1, \qquad (66)$$

where

$$B_0 = -k_1\frac{dL_1(r|l)}{dr}\bigg|_{r=a_0}, \qquad (67)$$

$$C_0 = k_1\frac{dR_1(r|l)}{dr}\bigg|_{r=a_0}. \qquad (68)$$

Next, using representations (64) in the second of conjunction conditions (28) at the interface $r = a_j$ between shells j and $j+1$ yields:

$$A_j(l)v_{j-1}(l) - C_j(l)v_j(l) + B_j(l)v_{j+1}(l) = 0 \qquad (69)$$
$$(j = 1, 2, \ldots, N-2)$$

with

$$A_j = k_j\frac{dR_j(r|l)}{dr}\bigg|_{r=a_j}, \qquad (70)$$

$$B_j = -k_{j+1}\frac{dL_{j+1}(r|l)}{dr}\bigg|_{r=a_j}, \qquad (71)$$

$$C_j = k_{j+1}\frac{dR_{j+1}(r|l)}{dr}\bigg|_{r=a_j} - k_j\frac{dL_j(r|l)}{dr}\bigg|_{r=a_j}. \quad (72)$$

Obviously, these equations apply only if $N \geq 3$.

Finally, substituting representations (64) for $j = N-1$ and (65) in the second of conjunction conditions (28) at the interface $r = a_{N-1}$ between shell $N-1$ and the core (layer N) leads to a relation

$$A_{N-1}(l)v_{N-2}(l) - C_{N-1}(l)v_{N-1}(l) = 0, \quad (73)$$

where

$$A_{N-1} = k_{N-1}\frac{dR_{N-1}(r|l)}{dr}\bigg|_{r=a_{N-1}}, \quad (74)$$

$$C_{N-1} = k_N\frac{dR_N(r|l)}{dr}|_{r=a_{N-1}} - k_{N-1}\frac{dL_{N-1}(r|l)}{dr}\bigg|_{r=a_{N-1}}. \quad (75)$$

Equations (66), (69), and (73) constitute a tridiagonal system of linear algebraic equations (SLAE) for the N unknowns (63). In terms of [56, 16], the SLAE in question is an exact discretized version of problem (26)–(29). Once the solution to the SLAE is known, the function $v(r|l)$ can be recovered at any point of the interval $0 \leq r \leq a$ via Eqs. (64), (65).

By Eqs. (57), (58), and (61), we have the following explicit formulas:

$$B_0(l) = \frac{k_1}{a_0}\frac{(2l+1)(a_1/a_0)^{l+1}}{1-(a_1/a_0)^{2l+1}}, \quad (76)$$

$$C_0(l) = \frac{k_1}{a_0}\frac{l+(l+1)(a_1/a_0)^{2l+1}}{1-(a_1/a_0)^{2l+1}}, \quad (77)$$

$$A_j(l) = \frac{k_j}{a_j}\frac{(2l+1)(a_j/a_{j-1})^{l}}{1-(a_j/a_{j-1})^{2l+1}}, \quad (78)$$

$$B_j(l) = \frac{k_{j+1}}{a_j}\frac{(2l+1)(a_{j+1}/a_j)^{l+1}}{1-(a_{j+1}/a_j)^{2l+1}}, \quad (79)$$

$$C_j(l) = \frac{k_{j+1}}{a_j}\frac{l+(l+1)(a_{j+1}/a_j)^{2l+1}}{1-(a_{j+1}/a_j)^{2l+1}} + \frac{k_j}{a_j}\frac{l+1+l(a_j/a_{j-1})^{2l+1}}{1-(a_j/a_{j-1})^{2l+1}}, \quad (80)$$

$$(j = 1, 2, \ldots, N-2)$$

$$A_{N-1}(l) = \frac{k_{N-1}}{a_{N-1}}\frac{(2l+1)(a_{N-1}/a_{N-2})^{l}}{1-(a_{N-1}/a_{N-2})^{2l+1}}, \quad (81)$$

$$C_{N-1}(l) = \frac{lk_N}{a_{N-1}} + \frac{k_{N-1}}{a_{N-1}}\frac{l+1+l(a_{N-1}/a_{N-2})^{2l+1}}{1-(a_{N-1}/a_{N-2})^{2l+1}}. \quad (82)$$

SLAE properties and solution procedure. One can easily see from the expressions immediately above that for $l = 1, 2, 3, \ldots$ the following inequalities hold:

$$C_0(l) > B_0(l) > 0, \quad (83)$$

$$C_j(l) > A_j(l) + B_j(l), \quad A_j(l) > 0, \quad B_j(l) > 0 \quad (84)$$

$$(j = 1, 2, \ldots, N-2)$$

$$C_{N-1}(l) > A_{N-1}(l) > 0. \quad (85)$$

In consequence of properties (83)–(85), for each admissible l, the coefficient matrix of SLAE (66), (69), (73) is strictly *diagonally dominant* by rows and, therefore, *non-singular* thus ensuring the uniqueness of solution to the considered SLAE[3]. As yet another consequence, the sufficient conditions for the applicability and *stability* of the Thomas, or tridiagonal matrix, algorithm are satisfied [44, § 1.1, Eq. (16)].

There are a number of variants of Thomas method, mostly based on implementation details or specific considerations [44, §§ 1.1, 1.2]. Our Eqs. (66), (69) and (73) can be most efficiently solved with the help of the left elimination variant of Thomas algorithm as follows [44, § 1.1, pp. 9–10]:

- start with

$$\sigma_{N-1}(l) = \frac{A_{N-1}(l)}{C_{N-1}(l)}, \quad (86)$$

  and calculate the coefficients $\{\sigma_j(l)\}_{j=1}^{N-2}$ using the *downward* recurrence relations

$$\sigma_j(l) = \frac{A_j(l)}{C_j(l) - \sigma_{j+1}(l)B_j(l)} \quad (87)$$

$$(j = N-2, \ldots, 2, 1)$$

  (the symbols σ_j have nothing to do with the surface 'charge density' in Eq. (3) and elsewhere!)

- calculate $\{v_j(l)\}_{j=0}^{N-1}$ using the starting value

$$v_0(l) = \frac{1}{C_0(l) - \sigma_1(l)B_0(l)} \quad (88)$$

  and the *upward* recurrence relation

$$v_j(l) = \sigma_j(l)v_{j-1}(l) \quad (j = 1, 2, \ldots, N-1) \quad (89)$$

The strength of our solution procedure for the induced electric field is the simplicity and stability of the aforementioned algorithm (i.e., roundoff errors in floating point arithmetic remain bounded).

By virtue of properties (83)–(85), it can be shown inductively, starting with $j = N-1$, that for all admissible j the numerators in the right-hand side of Eqs. (88 and (88) are nonzero:

$$C_j(l) - \sigma_{j+1}(l)B_j(l) > A_j > 0, \quad (90)$$

and the multipliers $\sigma_j(l)$ are *bounded* by

$$0 < \sigma_j(l) < 1. \quad (91)$$

Using (91) in (88), (89) we find that

$$0 < v_{N-1}(l) < \ldots < v_1(1) < v_0(l). \quad (92)$$

The Wolfram Mathematica implementation of the numerical-analytical solution described in this Section is provided in Modules 1 to 8 of the code supplement.

[3] Incidentally, for $l = 0$ the SLAE coefficient matrix at hand is *singular*, i.e., its determinant is zero.

3. NUMERICAL SOLUTION USING FINITE-DIFFERENCE APPROACH

This Section aims to provide a direct numerical algorithm for numerically solving the low-frequency potential V_b in a stratified conducting sphere. The goal is not to present novel findings, but to verify the analytical solutions derived in the preceding section and to develop a robust computational tool for efficient analysis of various practical exposure problems. To accomplish this, we use the classic FD method [44, 26], which offers robust algorithms, supports general models, and is relatively straightforward for programming. The program implementation of the FD approach is detailed in Modules 9 to 18 of the code supplement.

Without loss of generality, we focus on a scenario where the point source is positioned in free space on the positive z axis at a distance h from the sphere ($h > 0$), as specified in Eq. (46). Due to the symmetry this assumption introduces, we will exclude the variable ϕ from our consideration, and formulate the BVPs in the r-θ domain.

For this scenario, we first derive the exact representations of the scalar potential in terms of auxiliary functions U, $W_{\parallel}$, and $W_{\perp}$, and present the BVPs for these functions. We then discretize the BVPs by approximating each derivative in the continual formulation with a difference *quotient* at the grid nodes [44, 26]. In the grids utilized in our computer program (implemented in Wolfram Mathematica), the local discretization error resulting from these approximations exhibits a quadratic dependence on the size of both radial and angular cells.

We do not detail the entire discretization process here, as it would compromise readability. The reader can verify the FD approximations by substituting Taylor series expansions into the FD quotients, noting that the functions U, $W_{\parallel}$, and $W_{\perp}$ satisfy their respective PDEs.

3.1. Considered Continual BVPs

Surface charge density for point sources on the z axis. In the following discussion, we do not make assumptions about the internal structure of the conducting sphere, remaining within the framework of a general model with a general conductivity distribution $k(\mathbf{r})$.

If the source is a point charge q, we find from the appropriately adapted Eqs. (15) and (3), that the surface charge density $\sigma(\theta, \phi) = \sigma(\theta)$ becomes independent of ϕ, leading to the following expression for $\sigma(\theta)$:

$$\sigma(\theta) = q\tau(\theta), \tag{93}$$

where

$$\tau(\theta) = \frac{1}{4\pi a}\left[\frac{1}{a+h} - \frac{h(h+2a)}{[h^2 + 4a(a+h)\sin^2\frac{\theta}{2}]^{\frac{3}{2}}}\right]. \tag{94}$$

When the source is a point dipole with moment $\mathbf{p}$, the following steps are convenient: First, derive the scalar potential V_0 for the dipole positioned next to the sphere by applying the operation $\mathbf{p}\cdot\nabla'$ to the representation (15) for the scalar potential of an arbitrarily positioned charge with $q = 1$. Then, set the observation point on the z-axis as specified in Eq. (46), and finally, determine the surface charge density σ using Eq. (3).

The first step results in the following expression for the scalar potential of the dipole in free space:

$$\begin{aligned} V_0(\mathbf{r}) &= V^{(inc)}(\mathbf{r}) + \frac{1}{4\pi\varepsilon_0}\frac{\mathbf{p}_*\cdot\mathbf{n}_*}{|\mathbf{r}-\mathbf{r}_*|^2} \\ &\quad + \frac{1}{4\pi\varepsilon_0}\left[\frac{q_*}{|\mathbf{r}-\mathbf{r}_*|} + \frac{q_{**}}{r}\right], \end{aligned} \tag{95}$$

$$V^{(inc)}(\mathbf{r}) = \frac{1}{4\pi\varepsilon_0}\frac{\mathbf{p}\cdot\mathbf{n}}{|\mathbf{r}-\mathbf{r}'|^2}, \tag{96}$$

$$\mathbf{n} = \frac{\mathbf{r}-\mathbf{r}'}{|\mathbf{r}-\mathbf{r}'|}, \tag{97}$$

$$\mathbf{n}_* = \frac{\mathbf{r}-\mathbf{r}_*}{|\mathbf{r}-\mathbf{r}_*|}, \tag{98}$$

$$q_* = \frac{a\mathbf{p}\cdot\mathbf{e}_1'}{r'^2}, \tag{99}$$

$$q_{**} = -q_*, \tag{100}$$

$$\mathbf{p}_* = \left(\frac{a}{r'}\right)^3 [2\mathbf{e}_1'(\mathbf{p}\cdot\mathbf{e}_1') - \mathbf{p}]. \tag{101}$$

Representation (95) illustrates that the potential due to a point dipole is generated by image sources within the sphere, including a charge q_* and a dipole of electric moment $\mathbf{p}_*$ at the point $\mathbf{r}_*$, as well as a charge q_{**} at the center of the sphere [3, Prob. 3.36, pp. 38–39, 251–252, 45].

In the case where the dipole is located in free space on the positive z axis, as indicated by Eq. (46), the corresponding surface charge density $\sigma(\theta, \phi)$ can be expressed as:

$$\sigma(\theta,\phi) = (p_x\cos\phi + p_y\sin\phi)\tau_{\perp}(\theta) + p_z\tau_{\parallel}(\theta), \tag{102}$$

where the functions $\tau_{\perp}$ and $\tau_{\parallel}$ are both independent of ϕ. Their expressions are:

$$\tau_{\perp}(\theta) = -\frac{1}{4\pi}\frac{3h(h+2a)\sin\theta}{[h^2 + 4a(a+h)\sin^2\frac{\theta}{2}]^{\frac{5}{2}}}, \tag{103}$$

$$\begin{aligned} \tau_{\parallel}(\theta) &= -\frac{1}{4\pi a}\left[\frac{1}{(a+h)^2}\right. \\ &\quad \left. + \frac{2a(h^2+2ah+4a^2)\sin^2\frac{\theta}{2} - h^2(h+4a)}{\left[h^2 + 4a(a+h)\sin^2\frac{\theta}{2}\right]^{\frac{5}{2}}}\right]. \end{aligned} \tag{104}$$

Equation (102) parallels a similar expression (50) for the potential V_b within the sphere. Expressions (94), (103), and (104) clearly demonstrate that

$$\frac{d\tau(\theta)}{d\theta} = 0, \quad \frac{d\tau_{\parallel}(\theta)}{d\theta} = 0, \quad \tau_{\perp}(\theta) = 0 \quad (\theta = 0, \pi) \tag{105}$$

As a final point, to support further analysis, we provide asymptotic representations for $\tau(\theta)$, $\tau_{\parallel}(\theta)$, and $\tau_{\perp}(\theta)$ as $h \gg a$. These representations are as follows:

$$\tau(\theta) \approx -\frac{3\cos\theta}{4\pi h^2}. \tag{106}$$

$$\tau_{\perp}(\theta) \approx -\frac{3\sin\theta}{4\pi h^3}, \tag{107}$$

$$\tau_{\parallel}(\theta) \approx \frac{3\cos\theta}{2\pi h^3}. \tag{108}$$

As an aside, it is worth mentioning that Eqs. (106) and (108) resemble an expression [25, Eq. (1.12)], [57, Sec. 4.7.1, p. 144, Eq. (4.72)], [53, p. 205, Sec. 3.24, Eq. (27)], [21, Eq. (2.15)]:

$$\sigma(\theta,\phi) = 3\varepsilon_0 E_0 \cos\theta \tag{109}$$

for the induced charge density on the surface of an uncharged insulated PEC sphere embedded in a uniform electric field aligned with the z-axis:

$$\mathbf{E}^{(inc)} = \mathbf{z}_0 E_0, \tag{110}$$

where E_0 is a constant.

Model and BVPs. We now revert to the assumption made in Section 2.1 and consider a general *piecewise-smooth* conductivity function $k(r)$ ($k(r) > 0$). This is different from the earlier assumption in Section 2.4, which treated $k(r)$ as piecewise-constant. For an arbitrary point r ($0 < r < a$) inside the sphere, we can define two one-sided limits: $k(r-0)$ and $k(r+0)$. If r lies within the continuous portion of the medium, these limits coincide with the value of k at that particular point: $k(r-0) = k(r+0) = k(r)$. When the point r corresponds to an interface, it is possible for $k(r-0)$ to be different from $k(r+0)$. The precise positions of these interfaces are not detailed in this Section. To allow greater flexibility in subsequent derivations, we permit a situation where $k(r-0) = k(r+0)$ at an interface. In such a situation, the interface serves as a geometric concept rather than a separate material entity.

In order to address future needs, we will now introduce the following linear differential operators:

$$L^{(r)} \stackrel{\text{def}}{=} \frac{1}{k(r)}\frac{\partial}{\partial r} r^2 k(r) \frac{\partial}{\partial r}, \tag{111}$$

$$L^{(\theta)}(\nu) \stackrel{\text{def}}{=} \frac{1}{\sin\theta}\frac{\partial}{\partial\theta}\sin\theta\frac{\partial}{\partial\theta} - \frac{\nu^2}{\sin^2\theta}. \tag{112}$$

These operators act on the variables r and θ, respectively. The parameter ν in the definition of $L^{(\theta)}(\nu)$ can be either 0 or 1 in the forthcoming derivations. It is important to note that the symbols r and θ, when employed as superscripts, should be regarded solely as labels rather than representations of arguments or specific variable values.

In the scenario involving a point charge, based on the expression (93) for σ, the potential V_b inside the sphere can be expressed as a function independent of ϕ:

$$V_b = i\omega q U(r,\theta). \tag{113}$$

Thus, the initial formulation presented by Eqs. (4)–(7) can be reformulated in the r-θ plane as follows:

$$\left[L^{(r)} + L^{(\theta)}(0)\right] U(r,\theta) = 0 \quad (0 < r < a,\ 0 < \theta < \pi) \tag{114}$$

$$k(r)\frac{\partial U(r,\theta)}{\partial r} = \tau(\theta) \quad (r = a) \tag{115}$$

$$\frac{\partial U(r,\theta)}{\partial\theta} = 0 \quad (\theta = 0,\pi; \quad 0 < r < a) \tag{116}$$

$$\{U(r,\theta)\} = 0, \quad \left\{k(r)\frac{\partial U(r,\theta)}{\partial r}\right\} = 0 \tag{117}$$

$$U(r,\theta) = 0 \quad (r = 0) \tag{118}$$

The PDE (114) does not apply to the values of r where the coefficients of the PDE, such as the function $k(r)$ or its first derivative, are discontinuous. These points represent the interfaces in our formulation. For each interface, the interface conditions from (117) are applied. The boundary condition (115) and the symmetry condition (116) are derived from Eq. (5) and the first relation in Eq. (105), respectively. The condition at the origin, given in Eq. (118), addresses the requirement for boundedness and also ensures uniqueness by specifying that the desired potential must be zero at the origin.

In the scenario involving a point dipole, using representations (50) and (102), we derive the BVPs in the r-θ plane for the functions $W_{\perp}$ and $W_{\parallel}$ from Eqs. (4)–(7). Specifically, the function $W_{\parallel}$ satisfies a BVP that is formally derived from Eqs. (114)–(118) after replacing $U \to W_{\parallel}$ and $\tau \to \tau_{\parallel}$. The function $W_{\perp}$ satisfies the following BVP:

$$\left[L^{(r)} + L^{(\theta)}(1)\right] W_{\perp}(r,\theta) = 0 \quad (0<r<a,\ 0<\theta<\pi) \tag{119}$$

$$k(r)\frac{\partial W_{\perp}(r,\theta)}{\partial r} = \tau_{\perp}(\theta) \quad (r = a) \tag{120}$$

$$W_{\perp}(r,\theta) = 0 \quad (\theta = 0,\pi; \quad 0 < r < a) \tag{121}$$

$$\{W_{\perp}(r,\theta)\} = 0, \quad \left\{k(r)\frac{\partial W_{\perp}(r,\theta)}{\partial r}\right\} = 0 \tag{122}$$

$$W_{\perp}(r,\theta) \to 0 \quad (r \to 0) \tag{123}$$

We do not elaborate on the mathematical significance of the components in this BVP, as they parallel those in Eqs. (114)–(118).

A principal difference between the problems for U and $W_{\perp}$ lies in the fact that, at $\theta = 0,\pi$, the functions U and $W_{\perp}$ adhere to the Neumann and Dirichlet boundary conditions, respectively — see Eqs. (116) and (121). Similarly, the problems for U and $W_{\parallel}$ can be categorized as the same type since both require the Neumann boundary conditions at $\theta = 0,\pi$.

3.2. FD Discretization for U and $W_\perp$

In this section, we will outline the discretization algorithm for the representative continual BVPs, specifically (114)–(118) for U and (119)–(123) for $W_\perp$. To maintain brevity, we will omit the discretization scheme for the BVP for $W_\parallel$, as it follows the same structure as the one for U.

FD grids. To discretize the radial coordinate, we split up the interval $0 \le r \le a$ into M subintervals $[r_m, r_{m-1}]$ by the $M+1$ nodes

$$0 = r_M < r_{M-1} < \ldots < r_1 < r_0 = a \tag{124}$$

such that they *include* all of the interface points as a subset. The precise locations of these interfaces are not explicitly specified in this Section. The set of indexes m associated with the *interfaces* is denoted as $\mathcal{M}$.

Note that we enumerate the radial nodes starting from the outermost node (r_0) and proceed *inwards*. The length of grid cell $[r_m, r_{m-1}]$ ($m = 1, 2, \ldots, M$) is represented by $\Delta r_m = r_{m-1} - r_m$. The parts $[r_m, r_{m-1}]$ need not be of equal length (the *non-uniform* grid). A non-uniform radial grid enables grid adaptation to enhance resolution by adjusting the cell size in each layer and incorporating smaller spacing between grid cells near the center of the sphere, while utilizing larger grid cells elsewhere. In our program implementation of the FD algorithm, the radial grid is uniform within each layer; however, the grid size may vary across layers.

The angular domain $0 \le \theta \le \pi$ is discretized by introducing a *uniformly* partitioned angular grid with the nodes

$$\theta_n = n\Delta\theta \quad (n = 0, 1, 2, \ldots, N) \tag{125}$$

$$\Delta\theta = \frac{\pi}{N}. \tag{126}$$

Please note that in this Section, the notation N refers to the discretization of the angular coordinate, where $N+1$ represents the number of nodes in the angular domain. It is important to clarify that this definition of N is unrelated to a similar symbol used in previous Sections, where it represents the number of layers composing the stratified sphere. Although the use of the same symbol may appear duplicated, it is hoped that this does not introduce any ambiguity, as the number of layers is not explicitly relevant in this particular Section.

For the grid in the r-θ domain, the grid nodes (r_m, θ_n) are assigned two indices: $m = 0, 1, 2, \ldots, M$ for the radial direction, and $n = 0, 1, 2, \ldots, N$ for the polar angle direction. As customary, the subscripts will accompany the value of a function at the corresponding grid node: $k_m = k(r_m)$, $\tau_n = \tau(\theta_n)$, $U_{mn} = U(r_m, \theta_n)$.

In the FD equations presented below, we include error terms for clarity. The actual FD approximations are obtained by discarding these error terms. We first present the discretized equations for the function U and then outline those for $W_\perp$.

Discretization of PDE (114). When the node r_m falls within a continuous layer (i.e., the index m does *not* belong to the set $\mathcal{M}$), and θ_n is a point *inside* the interval $0 < \theta < \pi$ (i.e., $n = 1, 2, 3, \ldots, N-1$), the FD approximation of the PDE (114) can be expressed as

$$A_m^{(r)} U_{m-1,n} - \left[C_m^{(r)} + C_n^{(\theta)}(0)\right] U_{mn} + B_m^{(r)} U_{m+1,n} + A_n^{(\theta)} U_{m,n-1} + B_n^{(\theta)} U_{m,n+1} + \epsilon_m^{(r)} + \mathcal{O}(\Delta\theta^2) = 0 \tag{127}$$
$$(m = 1, 2, 3, \ldots, M-1 \ \wedge \ m \notin \mathcal{M} \ \wedge \ n = 1, 2, 3, \ldots, N-1)$$

with

$$A_m^{(r)} = \frac{(k_{m-1} + k_m)(r_m + \Delta r_m/2)^2}{k_m \Delta r_m (\Delta r_m + \Delta r_{m+1})}, \tag{128}$$

$$B_m^{(r)} = \frac{(k_m + k_{m+1})(r_m - \Delta r_{m+1}/2)^2}{k_m \Delta r_{m+1} (\Delta r_m + \Delta r_{m+1})}, \tag{129}$$

$$C_m^{(r)} = A_m^{(r)} + B_m^{(r)}, \tag{130}$$

$$A_n^{(\theta)} = \frac{\sin\theta_{n-1} + \sin\theta_n}{2\Delta\theta^2 \sin\theta_n}, \tag{131}$$

$$B_n^{(\theta)} = \frac{\sin\theta_n + \sin\theta_{n+1}}{2\Delta\theta^2 \sin\theta_n}, \tag{132}$$

$$C_n^{(\theta)}(0) = A_n^{(\theta)} + B_n^{(\theta)}. \tag{133}$$

$$\epsilon_m^{(r)} = \begin{cases} \mathcal{O}(\Delta r_m) + \mathcal{O}(\Delta r_{m+1}) & (\Delta r_{m+1} \ne \Delta r_m) \\ \mathcal{O}(\Delta r_m^2) & (\Delta r_{m+1} = \Delta r_m) \end{cases} \tag{134}$$

The aforementioned expressions for $A_m^{(r)}$ and $B_m^{(r)}$ are predicated on the assumption that both nodes r_{m+1} and r_{m-1},

$$r_{m+1} = r_m - \Delta r_{m+1}, \quad r_{m-1} = r_m + \Delta r_m, \tag{135}$$

reside *inside* the designated layer. However, in the event that either node r_{m+1} and/or r_{m-1} resides at the interface between the designated layer and an adjoining layer, it becomes necessary to modify the aforementioned formulas for $A_m^{(r)}$ and $B_m^{(r)}$. This modification involves replacing the respective function values k_{m+1} or k_{m-1} with a one-sided limit. Specifically, k_{m+1} should be replaced with $k(r_{m+1} + 0)$ and k_{m-1} with $k(r_{m-1} - 0)$ as appropriate.

Discretization of Boundary Condition (115). When considering a radial node r_m on the boundary $r = a$ (i.e., $m = 0$), it is necessary to differentiate between two scenarios: one where the angular node θ_n is a point *inside* the interval $0 < \theta < \pi$ (i.e., $n = 1, 2, 3, \ldots, N-1$), and another where the node θ_n is the *endpoint* 0 or π (i.e., $n =$ or $n = N$).

In the former situation, the FD approximation of the boundary condition (115) can be expressed as:

$$-\left[B_0^{(r2)} + \frac{\Delta r_1 k_0^{(-)}}{2r_0^2} C_n^{(\theta)}(0)\right] U_{0n} + B_0^{(r2)} U_{1n} + \frac{\Delta r_1 k_0^{(-)}}{2r_0^2} \left(A_n^{(\theta)} U_{0,n-1} + B_n^{(\theta)} U_{0,n+1}\right) + \mathcal{O}(\Delta r_1^2) + \mathcal{O}(\Delta r_1 \Delta\theta^2) = -\tau_n \tag{136}$$
$$(m = 0 \quad \wedge \quad n = 1, 2, 3, \ldots, N-1)$$

Here we have defined

$$k_0^{(-)} = k(r_0 - 0), \tag{137}$$

$$B_0^{(r2)} = \frac{2(r_0-\Delta r_1/2)^2 k_1 k_0^{(-)}}{r_0^2 \Delta r_1 \left(k_1+k_0^{(-)}\right)}, \quad (138)$$

$$B_0^{(\theta)} = A_N^{(\theta)} = \frac{4}{\Delta\theta^2}. \quad (139)$$

The corresponding difference equations at the angular end nodes θ_0 and θ_N (where $\theta_0 = 0$ and $\theta_N = \pi$) are as follows:

$$-\left(B_0^{(r2)} + \frac{\Delta r_1 k_0^{(-)}}{2r_0^2} B_0^{(\theta)}\right) U_{00} + B_0^{(r2)} U_{10}$$

$$+\frac{\Delta r_1 k_0^{(-)}}{2r_0^2} B_0^{(\theta)} U_{01} + \mathcal{O}(\Delta r_1^2) + \mathcal{O}(\Delta r_1 \Delta\theta^2) = -\tau_0 \quad (140)$$

$$(m=0 \quad \wedge \quad n=0)$$

and

$$-\left(B_0^{(r2)} + \frac{\Delta r_1 k_0^{(-)}}{2r_0^2} A_N^{(\theta)}\right) U_{0N} + B_0^{(r2)} U_{1N}$$

$$+\frac{\Delta r_1 k_0^{(-)}}{2r_0^2} A_N^{(\theta)} U_{0,N-1} + \mathcal{O}(\Delta r_1^2) + \mathcal{O}(\Delta r_1 \Delta\theta^2) = -\tau_N \quad (141)$$

$$(m=0 \quad \wedge \quad n=N)$$

Equations (140) and (141) have been derived considering the property

$$\frac{\partial^3 U(r,\theta)}{\partial\theta^3} = 0 \quad (\theta = 0, \pi; \quad 0 < r < a) \quad (142)$$

which the function $U(r,\theta)$ exhibits due to the first relation in Eq. (105).

Discretization of interface conditions (117). We focus here on the case where the node r_m is situated at an interface (i.e., $m \in \mathcal{M}$). Since the radial node is positioned at the interface, the continuity of $U(r,\theta)$ specified by the first condition in Eq. (117) is enforced automatically. The discretized version of the second condition in Eq. (117) at every *interior* angular node θ_n (where n ranges from 1 to $N-1$) is given by:

$$A_m^{(r2)} U_{m-1,n} - \left[C_m^{(r2)} + \left(\frac{\Delta r_m k_m^{(+)}}{2r_m^2} + \frac{\Delta r_{m+1} k_m^{(-)}}{2r_m^2}\right) C_n^{(\theta)}(0)\right] U_{mn}$$

$$+B_m^{(r2)} U_{m+1,n} + \left(\frac{\Delta r_m k_m^{(+)}}{2r_m^2} + \frac{\Delta r_{m+1} k_m^{(-)}}{2r_m^2}\right)$$

$$\left(A_n^{(\theta)} U_{m,n-1} + B_n^{(\theta)} U_{m,n+1}\right) + \mathcal{O}(\Delta r_m^2) + \mathcal{O}(\Delta r_{m+1}^2)$$

$$+\mathcal{O}(\Delta r_m \Delta\theta^2) + \mathcal{O}(\Delta r_{m+1}\Delta\theta^2) = 0 \quad (143)$$

$$(m \in \mathcal{M} \quad \wedge \quad n = 1,2,3,\ldots,N-1)$$

where

$$A_m^{(r2)} = \frac{2(r_m+\Delta r_m/2)^2 k_{m-1} k_m^{(+)}}{r_m^2 \Delta r_m \left(k_{m-1}+k_m^{(+)}\right)}, \quad (144)$$

$$B_m^{(r2)} = \frac{2(r_m-\Delta r_{m+1}/2)^2 k_{m+1} k_m^{(-)}}{r_m^2 \Delta r_{m+1} \left(k_{m+1}+k_m^{(-)}\right)}, \quad (145)$$

$$C_m^{(r2)} = A_m^{(r2)} + B_m^{(r2)}, \quad (146)$$

and $k_m^{(-)}$ and $k_m^{(+)}$ represent the limits of the function $k(r)$ as the argument r approaches the node r_m from below or above, respectively:

$$k_m^{(-)} = k(r_m - 0), \quad k_m^{(+)} = k(r_m + 0). \quad (147)$$

Discretization of symmetry condition (116). For the *interior* radial nodes r_m ($m = 1,2,3,\ldots,M-1$) that do *not* belong to the interfaces (i.e., $m \notin \mathcal{M}$), the discretized version of the symmetry condition (116) takes the following form: at the angular end node $\theta = \theta_0$ —

$$\frac{\Delta\theta}{4} A_m^{(r)} U_{m-1,0} - \left(B_0^{(\theta 1)} + \frac{\Delta\theta}{4} C_m^{(r)}\right) U_{m0}$$

$$+\frac{\Delta\theta}{4} B_m^{(r)} U_{m+1,0} + B_0^{(\theta 1)} U_{m1} + \epsilon_{m0}^{(r\theta)} = 0 \quad (148)$$

$$(m = 1,2,3,\ldots,M-1 \quad \wedge \quad m \notin \mathcal{M} \quad \wedge \quad n = 0)$$

and at the angular end node $\theta = \theta_N$ —

$$-\frac{\Delta\theta}{4} A_m^{(r)} U_{m-1,N} + \left(A_N^{(\theta 1)} + \frac{\Delta\theta}{4} C_m^{(r)}\right) U_{mN}$$

$$-\frac{\Delta\theta}{4} B_m^{(r)} U_{m+1,N} - A_N^{(\theta 1)} U_{m,N-1} + \epsilon_{mN}^{(r\theta)} = 0 \quad (149)$$

$$(m = 1,2,3,\ldots,M-1 \quad \wedge \quad m \notin \mathcal{M} \quad \wedge \quad n = N)$$

where

$$B_0^{(\theta 1)} = A_N^{(\theta 1)} = \frac{1}{\Delta\theta}. \quad (150)$$

The local discretization error $\epsilon_{m0}^{(r\theta)}$ in relation (148) is given by:

$$\epsilon_{m0}^{(r\theta)} = \mathcal{O}(\Delta\theta^3)$$

$$+\Delta\theta \cdot \begin{cases} \mathcal{O}(\Delta r_m) + \mathcal{O}(\Delta r_{m+1}) & (\Delta r_{m+1} \neq \Delta r_m) \\ \mathcal{O}(\Delta r_m^2) & (\Delta r_{m+1} = \Delta r_m) \end{cases} \quad (151)$$

(Note that the error term $\epsilon_{mN}^{(r\theta)}$ in Eq. (149) has the same form and is omitted here.)

When the radial node r_m is situated at an interface (i.e., $m \in \mathcal{M}$), the following discretized versions of the symmetry condition (116) apply: at the angular end node $\theta = \theta_0$ —

$$\frac{\Delta\theta}{2} \frac{r_m^2}{\Delta r_m k_m^{(+)} + \Delta r_{m+1} k_m^{(-)}} A_m^{(r2)} U_{m-1,0}$$

$$-\left(B_0^{(\theta 1)} + \frac{\Delta\theta}{2} \frac{r_m^2}{\Delta r_m k_m^{(+)} + \Delta r_{m+1} k_m^{(-)}} C_m^{(r2)}\right) U_{m0}$$

$$+\frac{\Delta\theta}{2} \frac{r_m^2}{\Delta r_m k_m^{(+)} + \Delta r_{m+1} k_m^{(-)}} B_m^{(r2)} U_{m+1,0} + B_0^{(\theta 1)} U_{m1}$$

$$+\mathcal{O}(\Delta r_m \Delta\theta) + \mathcal{O}(\Delta r_{m+1}\Delta\theta) + \mathcal{O}(\Delta\theta^3) = 0 \quad (152)$$
$$(m \in \mathcal{M} \quad \wedge \quad n = 0)$$

and the angular end node $\theta = \theta_N$ —

$$\frac{\Delta\theta}{2}\frac{r_m^2}{\Delta r_m k_m^{(+)} + \Delta r_{m+1} k_m^{(-)}} A_m^{(r2)} U_{m-1,N}$$
$$-\left(A_N^{(\theta 1)} + \frac{\Delta\theta}{2}\frac{r_m^2}{\Delta r_m k_m^{(+)} + \Delta r_{m+1} k_m^{(-)}} C_m^{(r2)}\right) U_{mN}$$
$$+\frac{\Delta\theta}{2}\frac{r_m^2}{\Delta r_m k_m^{(+)} + \Delta r_{m+1} k_m^{(-)}} B_m^{(r2)} U_{m+1,N} + A_N^{(\theta 1)} U_{m,N-1}$$
$$+\mathcal{O}(\Delta r_m \Delta\theta) + \mathcal{O}(\Delta r_{m+1}\Delta\theta) + \mathcal{O}(\Delta\theta^3) = 0 \quad (153)$$
$$(m \in \mathcal{M} \quad \wedge \quad n = N)$$

Relations (148)–(149) and (152)–(153) were derived under the assumption that the radial cell sizes Δr_m and Δr_{m+1} are of the same order of magnitude:

$$\mathcal{O}\left(\frac{\Delta r_m}{\Delta r_{m+1}}\right) = 1. \quad (154)$$

Additionally, property (142) was considered in the derivations.

Discretization of the condition at the origin (118). The discrete version of Eq. (118) is evident:

$$U_{M0} = 0 \quad (155)$$
$$(m = M \quad \wedge \quad n = 0)$$

When formulating this relation, we acknowledge that the $N+1$ points (r_M, θ_n) in the r-θ plane, where $n = 0, 1, 2, \ldots, N$, correspond to the identical node. In Eq. (155), we have selected $n = 0$ to simplify the indexing of unknowns and equations with a single index [26, Sec. 2.14].

Discretization of BVP (119)–(123) for $W_\perp$. For the sake of clarity in subsequent notation, we will refer to the function $W_\perp$ as W, and the function $\tau_\perp$ from boundary condition (120) as τ.

The discretized versions of PDE (119), the second interface condition in Eq. (122), and the boundary condition (120) at the interior angular nodes θ_n (where $n = 1, 2, 3, \ldots, N-1$) are similar to their respective equations (127), (143), and (136) for U, except that the coefficient $C_n^{(\theta)}(0)$ must be replaced by $C_n^{(\theta)}(1)$:

$$C_n^{(\theta)}(1) = A_n^{(\theta)} + B_n^{(\theta)} + \frac{1}{\sin^2\theta_n}. \quad (156)$$

The difference equations that correspond to the boundary condition (120) at the angular end nodes θ_0 and θ_N are given by:

$$-B_0^{(r2)} W_{00} + B_0^{(r2)} W_{10} + \mathcal{O}(\Delta r_1^2) = -\tau_0 \quad (157)$$
$$(m = 0 \quad \wedge \quad n = 0)$$

and

$$-B_0^{(r2)} W_{0N} + B_0^{(r2)} W_{1N} + \mathcal{O}(\Delta r_1^2) = -\tau_N \quad (158)$$
$$(m = 0 \quad \wedge \quad n = N)$$

These equations have been derived considering the property

$$\frac{\partial^2 W(r,\theta)}{\partial\theta^2} = 0 \quad (\theta = 0, \pi; \quad 0 < r < a) \quad (159)$$

which the function $W(r,\theta)$ exhibits due to the last relation in Eq. (105).

The symmetry condition (121) represents a Dirichlet condition, leading directly to:

$$W_{m0} = 0 \quad (m = 0, 1, 2, \ldots, M-1 \quad \wedge \quad n = 0) \quad (160)$$
$$W_{mN} = 0 \quad (m = 0, 1, 2, \ldots, M-1 \quad \wedge \quad n = N) \quad (161)$$

These equations incorporate the nodes (r_0, θ_0) (for $m = n = 0$), and (r_0, θ_N) (for $m = 0$, $n = N$).

Furthermore, the condition at the origin (123) leads to the same form (155) as the one for the function U.

3.3. Computation of the Induced Electric Field Vector on the FD Grid

We present the formulas required to approximate the induced electric field vector (2) on the FD grid in the r-θ plane. This approximation involves calculating the gradient components of the functions U, $W_\parallel$, and $W_\perp$ at the grid nodes. However, we focus on the functions U and $W_\perp$ U because the corresponding expressions for $W_\parallel$ identical to those for U.

∇U at the origin node. At the origin node (with node indices $m = M$ and $n = 0$), we have the following expression:

$$\nabla U|_{x=y=z=0} = \mathbf{z}_0 \frac{U_{M-1,0} - U_{M-1,N}}{2\Delta r_M} + \mathcal{O}(\Delta r_M^2). \quad (162)$$

The nodal values of $\frac{1}{\mathbf{r}}\frac{\partial \mathbf{U}}{\partial\theta}$ are computed as follows:

$$\left(\frac{1}{r}\frac{\partial U}{\partial\theta}\right)_{mn} \quad (163)$$
$$= \begin{cases} 0 & (n = 0, N) \\ \dfrac{U_{m,n+1} - U_{m,n-1}}{2r_m\Delta\theta} + \mathcal{O}(\Delta\theta^2) & (n = 1, 2, 3, \ldots, N-1) \end{cases} \quad (164)$$
$$(m = 0, 1, 2, \ldots, M-1)$$

In the right hand side of the above equation, the top expression comes from the symmetry condition (116), and the bottom line is the well-known central difference approximation of the first derivative of $U(r,\theta)$ with respect to θ.

Nodal values of $\frac{\partial \mathbf{U}}{\partial \mathbf{r}}$ on the outer boundary of the sphere. From Eq. (115), for nodes (r_m, θ_n) on the outer boundary of the sphere ($m = 0$), we have:

$$\left(\frac{\partial U(r,\theta)}{\partial r}\right)_{0n} = \frac{\tau_n}{k_0^-} \quad (165)$$
$$(m = 0 \quad \wedge \quad n = 0, 1, 2, \ldots, N) \quad (166)$$

Nodal values of $\frac{\partial \mathbf{U}}{\partial \mathbf{r}}$ at an interface: This involves considering the one-sided limits of $\partial U(r,\theta)/\partial r$ as $\mathbf{r}$ approaches the interface from one side, due to the fact that the derivative $\partial U/\partial r$

does not exist at interfaces where the conductivity, as a function of r, exhibits a jump discontinuity.

To formalize this, we consider the index m to be a member of the set $\mathcal{M}$. The adjacent nodes of the radial grid, r_{m+1} and r_{m-1}, reside in the layers bordering the interface defined by $r = r_m$. Specifically, r_{m-1} is situated inside the outer layer, which is closer to the boundary of the sphere, while r_{m+1} is positioned inside the inner layer, closer to the sphere's center.

We begin by focusing on the *interior* angular nodes θ_n (where $n = 1, 2, 3, \ldots, N-1$). The following expressions represent the one-sided derivatives:

$$\left.\frac{\partial U(r,\theta)}{\partial r}\right|_{r=r_m+0,\,\theta=\theta_n} = \frac{A_m^{(r2)}}{k_m^{(+)}}\left(U_{m-1,n} - U_{mn}\right) + \frac{\Delta r_m}{2r_m^2}\left[A_n^{(\theta)}U_{m,n-1} - C_n^{(\theta)}(0)U_{mn} + B_n^{(\theta)}U_{m,n+1}\right] + \mathcal{O}(\Delta r_m^2) + \mathcal{O}(\Delta r_m \Delta\theta^2), \tag{167}$$

$$\left.\frac{\partial U(r,\theta)}{\partial r}\right|_{r=r_m-0,\,\theta=\theta_n} = \frac{B_m^{(r2)}}{k_m^{(-)}}\left(U_{mn} - U_{m+1,n}\right) - \frac{\Delta r_{m+1}}{2r_m^2}\left[A_n^{(\theta)}U_{m,n-1} - C_n^{(\theta)}(0)U_{mn} + B_n^{(\theta)}U_{m,n+1}\right] + \mathcal{O}(\Delta r_{m+1}^2) + \mathcal{O}(\Delta r_{m+1} \Delta\theta^2), \tag{168}$$

where the coefficients $A_n^{(\theta)}$, $B_n^{(\theta)}$ and $C_n^{(\theta)}(0)$ are given by Eqs. (131)–(134).

The one-sided derivatives $\frac{\partial U(r,\theta)}{\partial r}|_{r=r_m\pm 0}$ at the angular *end nodes* $\theta = \theta_0, \theta_N$ are given as follows: on the outer side $r = r_m + 0$ of the interface $r = r_m$ —

$$\left.\frac{\partial U(r,\theta)}{\partial r}\right|_{r=r_m+0,\,\theta=\theta_0} = \frac{A_m^{(r2)}}{k_m^{(+)}}\left(U_{m-1,0} - U_{m0}\right) + \frac{\Delta r_m}{2r_m^2}B_0^{(\theta)}\left(U_{m1} - U_{m0}\right) + \mathcal{O}(\Delta r_m^2) + \mathcal{O}(\Delta r_m \Delta\theta^2), \tag{169}$$

$$\left.\frac{\partial U(r,\theta)}{\partial r}\right|_{r=r_m+0,\,\theta=\theta_N} = \frac{A_m^{(r2)}}{k_m^{(+)}}\left(U_{m-1,N} - U_{mN}\right) + \frac{\Delta r_m}{2r_m^2}A_N^{(\theta)}\left(U_{m,N-1} - U_{mN}\right) + \mathcal{O}(\Delta r_m^2) + \mathcal{O}(\Delta r_m \Delta\theta^2), \tag{170}$$

and on the inner side $r = r_m - 0$ of the interface $r = r_m$ —

$$\left.\frac{\partial U(r,\theta)}{\partial r}\right|_{r=r_m-0,\theta=\theta_0} = \frac{B_m^{(r2)}}{k_m^{(-)}}\left(U_{m0} - U_{m+1,0}\right) - \frac{\Delta r_{m+1}}{2r_m^2}B_0^{(\theta)}\left(U_{m1} - U_{m0}\right) + \mathcal{O}(\Delta r_{m+1}^2) + \mathcal{O}(\Delta r_{m+1} \Delta\theta^2), \tag{171}$$

$$\left.\frac{\partial U(r,\theta)}{\partial r}\right|_{r=r_m-0,\theta=\theta_N} = \frac{B_m^{(r2)}}{k_m^{(-)}}\left(U_{mN} - U_{m+1,N}\right) - \frac{\Delta r_{m+1}}{2r_m^2}A_N^{(\theta)}\left(U_{m,N-1} - U_{mN}\right) + \mathcal{O}(\Delta r_{m+1}^2) + \mathcal{O}(\Delta r_{m+1} \Delta\theta^2), \tag{172}$$

where the coefficients $B_0^{(\theta)}$ and $A_N^{(\theta)}$ are defined in Eq. (139). The equations for the angular endpoints have been derived considering the property indicated by Eq. (142).

Nodal values of $\frac{\partial \mathbf{U}}{\partial \mathbf{r}}$ outside interfaces. For a non-origin node (r_m, θ_n) within a continuous medium, not at an interface ($m \notin \mathcal{M}$), the method applied to interface nodes can be used by treating the surface $r = r_m$ as a pseudo-interface where the function $k(r)$ remains continuous: $k(r_m - 0) = k(r_m + 0) = k(r_m)$.

If $\Delta r_{m+1} = \Delta r_m$, the derivative $\partial U(r,\theta)/\partial r$ at a non-origin node (r_m, θ_n) within the continuous medium can also be expressed as:

$$\left(\frac{\partial U(r,\theta)}{\partial r}\right)_{mn} = \frac{U_{m-1,n} - U_{m+1,n}}{2\Delta r_m} + \mathcal{O}(\Delta r_m^2), \tag{173}$$

which involves a well-known central difference approximation. This expression assumes that the nodes r_{m-1} and r_{m+1} are part of the same continuous medium as r_m.

The utility of this approximation is increased by the flexibility to introduce a mathematical interface at a given $r = r_m$, along with the corresponding interface conditions (117). The adjacent layers in the r variable can then be discretized, employing a specific *uniform* radial grid for each layer.

Horizontal dipole: Electric field at the origin node. We will now transition to the scenario involving a horizontal dipole, positioned outside the sphere on the z-axis, with its electric dipole moment perpendicular to the z-axis:

$$\mathbf{p} = \mathbf{x}_0 p_x + \mathbf{y}_0 p_y, \tag{174}$$

where p_x and p_y are complex numbers.

For ease of notation, we will refer to the function $W_\perp$ as W, and the function $\tau_\perp$ from boundary condition (120) as τ.

At the origin ($r = 0$), the electric field vector is characterized by the following expressions:

$$E_x(\mathbf{r})|_{x=y=z=0} = -i\omega p_x \left.\frac{\partial W(r, \frac{\pi}{2})}{\partial r}\right|_{r=0}, \tag{175}$$

$$E_y(\mathbf{r})|_{x=y=z=0} = -i\omega p_y \left.\frac{\partial W(r, \frac{\pi}{2})}{\partial r}\right|_{r=0}, \tag{176}$$

$$E_z(\mathbf{r})|_{x=y=z=0} = 0. \tag{177}$$

Using an FD approximation for the derivative $\frac{\partial W(r,\frac{\pi}{2})}{\partial r}|_{r=0}$, at the origin node (with the radial node index $m = M$), we derive:

$$\left.\frac{\partial W(r, \frac{\pi}{2})}{\partial r}\right|_{r=0} = -\frac{W(r_{M-1}, \frac{\pi}{2})}{\Delta r_M} + \mathcal{O}(\Delta r_M^2), \tag{178}$$

where we use the fact that $W(r_M, \frac{\pi}{2}) = 0$, as stated in Eq. (123).

When computing the value $W(r_{M-1}, \frac{\pi}{2})$ on the right-hand side of Eq. (178), we distinguish between two cases depending on whether the maximal angular nodal index N is even or odd.

In the case of N being even, we have $N = 2K$, where K is a natural number, and the angular value $\theta = \frac{\pi}{2}$ coincides with the angular node θ_K. Therefore, the quantity $W(r_{M-1}, \frac{\pi}{2})$ coincides with the nodal value $W_{M-1,K}$ on the 2D FD grid. Consequently,

$$\left.\frac{\partial W(r, \frac{\pi}{2})}{\partial r}\right|_{r=0} = -\frac{W_{M-1,K}}{\Delta r_M} + \mathcal{O}(\Delta r_M^2). \quad (179)$$

In the case of N being odd, we have $N = 2K+1$, where K is a natural number, and the angular value $\theta = \frac{\pi}{2}$ is located midway between the angular nodes θ_K and θ_{K+1}:

$$\frac{\pi}{2} = \frac{1}{2}\left(\theta_K + \theta_{K+1}\right). \quad (180)$$

Since $\frac{\pi}{2}$ is not an angular node, the quantity $W(r_{M-1}, \frac{\pi}{2})$ has to be estimated in terms of the nodal values $W(r_{M-1}, \theta_K) = W_{M-1,K}$ and $W(r_{M-1}, \theta_{K+1}) = W_{M-1,K+1}$ via linear interpolation as:

$$W\left(r_{M-1}, \frac{\pi}{2}\right) = \frac{1}{2}\left(W_{M-1,K} + W_{M-1,K+1}\right) + \mathcal{O}(\Delta\theta^2). \quad (181)$$

Substituting expression (181) for $W(r_{M-1}, \frac{\pi}{2})$ into Eq. (178) yields:

$$\left.\frac{\partial W(r, \frac{\pi}{2})}{\partial r}\right|_{r=0} = -\frac{W_{M-1,K} + W_{M-1,K+1}}{2\Delta r_M} + \mathcal{O}(\Delta r_M^2) + \mathcal{O}(\Delta\theta^2). \quad (182)$$

With the origin node addressed in the preceding discussion, we will now consistently refer, without explicit mention each time, to nodes (r_m, θ_n) that are not situated at the origin.

The nodal values of $\frac{1}{\mathbf{r}}\frac{\partial \mathbf{W}}{\partial \theta}$ are computed as follows:

$$\left(\frac{1}{r}\frac{\partial W}{\partial \theta}\right)_{mn} = \begin{cases} \dfrac{W_{m1}}{r_m \Delta\theta} & (n = 0) \\ \dfrac{W_{m,n+1} - W_{m,n-1}}{2 r_m \Delta\theta} & (n = 1, 2, 3, \ldots, N-1) \\ -\dfrac{W_{m,N-1}}{r_m \Delta\theta} & (n = N) \end{cases} + \mathcal{O}(\Delta\theta^2) \quad (m = 0, 1, 2, \ldots, M-1) \quad (183)$$

In the right-hand side of the above equation, the top and bottom expressions arise from the symmetry condition (121) and property (159) of the function W. The second line involves the well-known central difference approximation of the first derivative of $W(r, \theta)$ with respect to θ.

Nodal values of $\frac{\partial \mathbf{W}}{\partial \mathbf{r}}$ at the outer boundary of the sphere are determined by a formula similar to Eq. (165) for U. Note that according to the last expression in Eq. (105), we have $\tau_0 = \tau_N = 0$, which leads to:

$$\left(\frac{\partial W(r, \theta)}{\partial r}\right)_{0n} = 0 \quad (m = 0 \quad \wedge \quad n = 0, N) \quad (184)$$

Nodal values of $\frac{\partial \mathbf{W}}{\partial \mathbf{r}}$ at an interface. For the node (r_m, θ_n) at an interface ($m \in \mathcal{M}$), expressions for the one-sided derivatives $\frac{\partial W(r,\theta)}{\partial r}|_{r=r+m\pm 0}$ at interior angular nodes θ_n (where $n = 1, 2, 3, \ldots, N-1$) are similar to those for $\frac{\partial U(r,\theta)}{\partial r}|_{r=r+m\pm 0}$ in Eqs. (167)–(168), except that the coefficient $C_n^{(\theta)}(0)$ must be replaced by $C_n^{(\theta)}(1)$.

For the angular *end nodes* $\theta = \theta_0, \theta_N$, due to symmetry condition (121), the following exact relations hold:

$$\left.\frac{\partial W(r, \theta_n)}{\partial r}\right|_{r=r_m \pm 0} = 0 \quad (m \in \mathcal{M} \quad \wedge \quad n = 0, N) \quad (185)$$

Nodal values of $\frac{\partial \mathbf{W}}{\partial \mathbf{r}}$ outside interfaces. For a non-origin node (r_m, θ_n) located within the continuous medium *outside* the interfaces ($m \notin \mathcal{M}$), we can apply the methodology and expressions as previously used for the function U. Specifically, we can either treat the surface $r = r_m$, where the node is located, as a pseudo-interface where the function $k(r)$ remains continuous, applying the expressions for the one-sided derivatives, or we can use an expression similar to Eq. (173) for U.

Additionally, at the angular *end nodes* θ_0 and θ_N, due to symmetry condition (121), the following exact relations hold:

$$\left(\frac{\partial W(r, \theta_n)}{\partial r}\right)_{mn} = 0 \quad (m \notin \mathcal{M} \quad \wedge \quad n = 0, N) \quad (186)$$

4. COMPUTATIONAL RESULTS

We illustrate the functionality of the numerical-analytical and FD solutions by examining a four-layer sphere model that simulates the human head at low frequencies [35]. The Wolfram Mathematica code for this model is provided in Modules 19A to 29 of the supplement. The four layers represent the scalp, skull, cerebrospinal fluid (CSF), and brain, listed from the outermost layer inward. The model parameters are summarized in Table 1. The point sources considered are located in free space on the positive z axis at a distance h from the sphere ($h > 0$), as specified in Eq. (46).

For simplicity, we do not attach the layer-specific index j to the quantities in the table. The outer radii of the layers, representing the value of a_{j-1} for layer j, are consistent with those in [33]. The dielectric constant ε_{rel} (equivalent to the real part of the complex relative permittivity) was calculated for each layer at a frequency of 200 kHz, using an online database of tissue dielectric properties [17]. This frequency is representative of portable WPT devices [13, 20], which generally operate at frequencies not exceeding a few hundred kHz. The conductivities of the layers were sourced from an online database

TABLE 1. Parameters of a four-layer spherical model of the human head.

Model parameters	Scalp	Skull	CSF	Brain
Layer index j	1	2	3	4
Outer radius of layer, m	0.09	0.085	0.08	0.079
Dielectric constant ε_{rel}	1100	204	109	2300
Conductivity k, $\mathrm{m}^{-1}\,\mathrm{ohm}^{-1}$	0.148	0.0179	1.88	0.375
Dissipation factor $D = k/\omega\varepsilon_0\varepsilon_{rel}$	12.1	7.9	1550.2	14.7
Penetration depth $d = (2/\omega\mu_0 k)^{1/2}$, m	3.0	9.0	0.8	1.9
Free-space wavelength λ_0, m	1499			

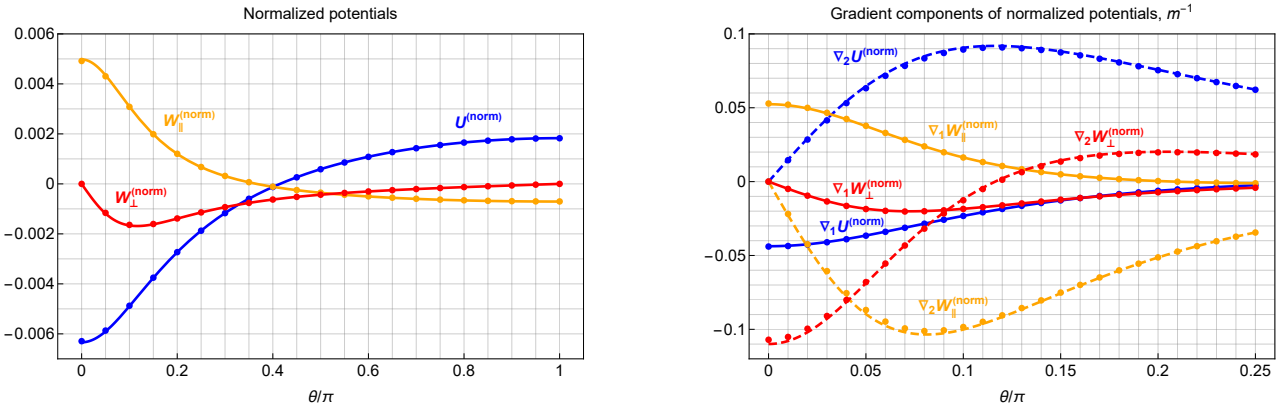

FIGURE 4. Angular profiles of the dimensionless normalized potentials, $U^{(\mathrm{norm})} = h^2 U$, $W_{\parallel}^{(\mathrm{norm})} = h^3 W_{\parallel}$, and $W_{\perp}^{(\mathrm{norm})} = h^3 W_{\perp}$, along with the spherical components of their gradients, defined by $\nabla_1 = \frac{\partial}{\partial r}$ and $\nabla_2 = \frac{1}{r}\frac{\partial}{\partial \theta}$. The profiles are evaluated at the midpoint of layer 3 (CSF) at $r = 0.0795$ m, with $h/a_0 = 0.3$.

of low-frequency conductivities [17]. Table 1 additionally includes key frequency-dependent characteristics of field-tissue interaction, namely the dissipation factor D (defined as the ratio of the conduction current to the displacement current) and the penetration depth d (the distance over which a plane wave in an unbounded medium attenuates by a factor of $e = 2.718\ldots$). The conditions for the low-frequency approximation used in this paper are [57, Sec. 13.10]:

$$D \gg 1, \quad d \gg a_0, \quad \lambda_0 \gg a_0, \tag{187}$$

where $\lambda_0 = 2\pi/\omega\sqrt{\epsilon_0\mu_0}$ is the free-space wavelength. These criteria are clearly met by the model presented.

The programmatic implementation of the solutions described in previous Sections has specific characteristics. In the case of the numerical-analytical solutions in Section 2, all summations involving l, as exemplified by formulas (24) and (40), have been *truncated* after $l = L_{\max}$. For the FD solution described in Section 3, the radial grid was defined by setting the number of *internal* nodes within each layer, in addition to radial nodes at each interface and the origin ($r = 0$). Our experiments with various combinations of these parameters confirmed the consistency and accuracy of the solutions.

In this Section, the results obtained from the EDS were computed using $L_{\max} = 40$, while the FD results were computed with a *uniform* distribution of radial nodes within each layer — specifically, 15 internal nodes in each of layers 1, 2, and 3, and 10 internal nodes (in addition to the origin node) in layer 4. The total number of angular nodes, including the end nodes at $\theta = 0$ and $\theta = \pi$, was 541. The total number of distinct nodes in the r-θ plane (equal to the number of unknowns) was 31,920. The resulting SLAE coefficient matrix contained 158,937 non-zero coefficients for the potentials U and $W_{\parallel}$, and 158,599 non-zero coefficients for the potential $W_{\perp}$. In the Wolfram Mathematica program that we developed, these SLAE coefficients were stored as a *SparseArray* object, and the SLAE was solved using the `LinearSolve[]` function.

Validation of solutions. Figures 4, 5, and 6 demonstrate the performance of the EDS solution (represented by solid and dashed lines) and the FD solution (shown as dots). The plots indicate that the agreement between these two solutions is quite strong.

In Fig. 4, the dimensionless quantities

$$U^{(norm)} = h^2 U, \quad W_{\parallel}^{(norm)} = h^3 W_{\parallel}, \quad W_{\perp}^{(norm)} = h^3 W_{\perp} \tag{188}$$

and the spherical components of their gradients are presented. The operators ∇_1 and ∇_2 are defined as

$$\nabla_1 = \frac{\partial}{\partial r}, \quad \nabla_2 = \frac{1}{r}\frac{\partial}{\partial \theta}. \tag{189}$$

These quantities are calculated as functions of the polar angle θ, with the distance $h = 0.3a_0$, and the radial variable set at $r =$

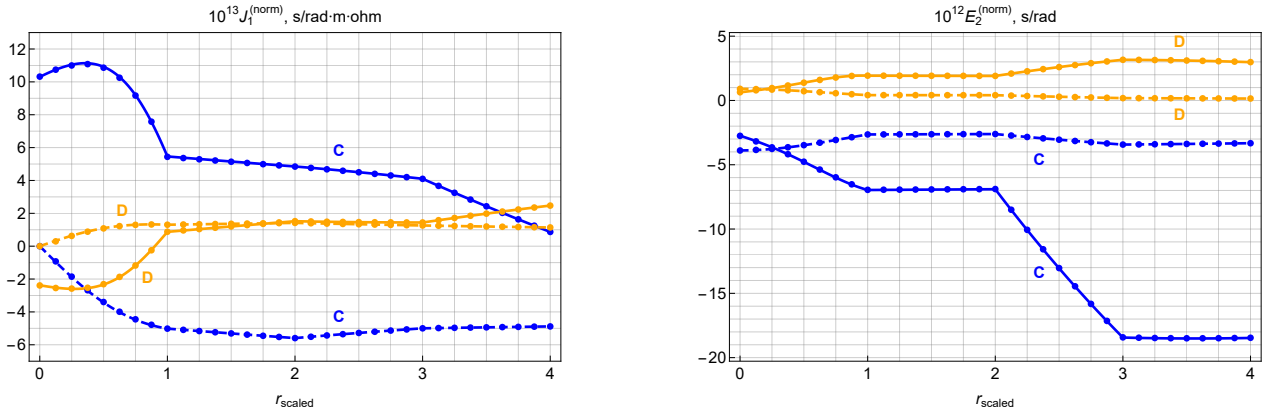

FIGURE 5. Radial profiles in terms of the scaled variable r_{scaled} (defined in Eq. (193)) for the radial component $J_1^{(\text{norm})}$ of the normalized conduction current density (Eq. (192)) and the transverse component $E_2^{(\text{norm})}$ of the normalized electric field (Eq. (190)). The excitation sources are a point charge (C) and a z-oriented dipole (D), both positioned at a distance h from the sphere ($h/a_0 = 0.3$). Profiles are shown for two polar angles: $\theta = \pi/4$ (solid lines and corresponding dots) and $\theta = \pi/2$ (dashed lines and corresponding dots). Solid and dashed lines represent EDS-based solutions, while dots indicate FD-based solutions.

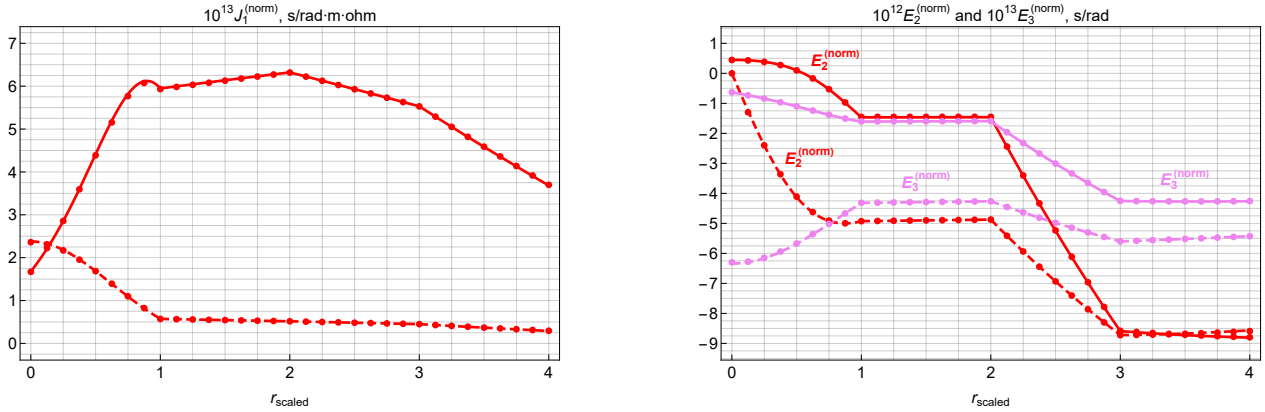

FIGURE 6. Radial profiles in terms of the scaled variable r_{scaled} (defined in Eq. (193)) for the radial component $J_1^{(\text{norm})}$ of the normalized conduction current density (Eq. (192)) and the transverse components $E_2^{(\text{norm})}$ and $E_3^{(\text{norm})}$ of the normalized electric field (Eq. (190)) induced by an x-oriented dipole located at a distance h from the sphere ($h/a_0 = 0.3$). Profiles are shown for a fixed azimuthal angle $\phi = \pi/4$ and two polar angles: $\theta = \pi/4$ (solid lines and corresponding dots) and $\theta = \pi/2$ (dashed lines and corresponding dots). Solid and dashed lines represent EDS-based solutions, while dots indicate FD-based solutions.

$(a_3 + a_4)/2$. This value determines a spherical surface within layer 3 (CSF), positioned midway between the outer boundary ($r = a_3$) and the inner boundary ($r = a_4$) of the layer. Layer 3 was chosen because it has the highest conductivity among all four layers, as indicated in Table 1.

Figure 5 shows the radial profiles (in terms of the *scaled* radial variable r_{scaled}) for the radial component $J_1^{(norm)}$ of the normalized conduction current density, and the transverse component $E_2^{(norm)}$ of the normalized electric field induced by a point charge (C) and a z-oriented dipole (D). Fig. 6 presents the radial profiles for $J_1^{(norm)}$ and the transverse components $E_2^{(norm)}, E_3^{(norm)}$ of the normalized electric field induced by an x-oriented dipole.

In both figures, the point sources are located at a distance $h = 0.3a_0$ from the sphere, with parameters q, p_z, and p_x assumed to be *real positive* values. Solid lines and their corresponding dots refer to the case where $\theta = \pi/4$, while dashed lines and their corresponding dots refer to the case where $\theta = \pi/2$. As mentioned earlier, lines correspond to EDS-based solutions, and dots represent FD solutions.

The normalized electric field in these plots, denoted as $\mathbf{E}^{(norm)}$, is defined as:

$$\mathbf{E}^{(norm)}(\mathbf{r}) = \frac{1}{\omega} \frac{\mathbf{E}(\mathbf{r})}{E_{\text{max}}^{(inc)}}, \tag{190}$$

where $E_{\text{max}}^{(inc)}$ represents the maximum magnitude of the incident electric field in a given excitation scenario, calculated over the region in free space corresponding to the conducting body in the excitation problem:

$$E_{\text{max}}^{(inc)} = \max_{0 \le r \le a_0} E^{(inc)}(\mathbf{r}). \tag{191}$$

It is crucial to note that the incident field and, therefore, $E_{\max}^{(inc)}$ pertain to a situation where *no* conducting sphere is present. The normalized conduction current density is defined as:

$$\mathbf{J}^{(norm)}(\mathbf{r}) = k(r)\mathbf{E}^{(norm)}(\mathbf{r}). \tag{192}$$

The division by ω in Eq. (190) makes the resulting normalized vectors $\mathbf{E}^{(norm)}(\mathbf{r})$ and $\mathbf{J}^{(norm)}(\mathbf{r})$ frequency independent, consistent with the low-frequency approximation. The division by $E_{\max}^{(inc)}$ reduces dependence on the corresponding parameters q, p_z, and p_x, as their absolute values are eliminated from both the numerator and denominator of the ratio $\mathbf{E}(\mathbf{r})/E_{\max}^{(inc)}$.

The components chosen for Figs. 5 and 6 are those that vary continuously with the radial variable, ensuring continuous plots. This contrasts with the transverse components of the conduction current and the radial component of the induced electric field, which display discontinuities at the interfaces.

To enhance clarity, the radial variable r_{scaled} has been introduced, which linearly transforms the radial intervals into scaled intervals of unit length. This transformation compensates for the varied thicknesses of the different layers, providing a cleaner representation. The interval $0 < r_{scaled} < 1$ corresponds to the brain (layer 4), $1 < r_{scaled} < 2$ to SCF (layer 3), $2 < r_{scaled} < 3$ to the skull (layer 2), and the interval $3 < r_{scaled} < 4$ to the scalp (layer 1). Mathematically, r_{scaled} is a continuous function of the variable r, defined for layers $j = 1, 2, 3, 4$ as follows:

$$r_{scaled}(r) = 4 - j + \frac{r - a_j}{a_{j-1} - a_j} \quad (a_j \le r \le a_{j-1}) \tag{193}$$

Physical characteristics of interaction. Our simulations focusing on physical aspects used the FD solutions and aimed at comparing the field and thermal coupling of incident electric fields to a conducting sphere for various sources, including point charges, linearly or circularly polarized dipoles, and uniform fields originating from infinitely remote sources. The FD approach was chosen for this study because it allows for an efficient search for the maximum values of the quantities of interest, namely, the magnitude of the induced electric field and the generated heat. Using the FD framework, this maximization is accomplished by comparing function values at the grid nodes in the r-θ domain, while maximizing over the ϕ variable (where present) analytically at each node.

When performing this search, a node at the interface $r = a_j$ (where $j = 1, 2, 3$) was considered twice — first as part of the inner layer $(j + 1)$, and then as part of the outer layer (j). This approach accounted for the discontinuity in the functions being maximized, specifically $E_{norm}(\mathbf{r})$ in Eq. (194) and $Q_{norm}(\mathbf{r})$ in Eq. (195), across the interface.

To characterize the physical effects associated with the transmission of an incident electric field into a conducting body, we can use the magnitude of the normalized induced electric field, $E_{norm}(\mathbf{r})$:

$$E_{norm}(\mathbf{r}) = \left|\mathbf{E}^{(norm)}(\mathbf{r})\right| \quad (\mathbf{r} \in \mathcal{B}) \tag{194}$$

This quantity is measured in units of $\mathrm{s\,rad^{-1}}$. Additionally, the normalized rate of heat generation, $Q_{norm}(\mathbf{r})$, can be defined as:

$$Q_{norm}(\mathbf{r}) = \frac{1}{2}k(r)E_{norm}^2(\mathbf{r}) \quad (\mathbf{r} \in \mathcal{B}) \tag{195}$$

This value is measured in units of $\mathrm{m^{-1}\,s^2\,ohm^{-1}\,rad^{-2}}$. It is related to the rate of heat generation, $Q(\mathbf{r})$, defined as:

$$Q(\mathbf{r}) = \frac{1}{2}k(r)\left|\mathbf{E}(\mathbf{r})\right|^2 \quad (\mathbf{r} \in \mathcal{B}) \tag{196}$$

The relationship between $Q_{norm}(\mathbf{r})$ and $Q(\mathbf{r})$ is given by:

$$Q_{norm}(\mathbf{r}) = \frac{1}{\omega^2}\frac{Q(\mathbf{r})}{E_{\max}^{(inc)2}}. \tag{197}$$

For a given incident field, the coupling coefficient for the electric field, K_E, is defined as the maximum magnitude of the normalized electric field within the conducting body:

$$K_E = \max_{\mathbf{r}\in\mathcal{B}} E_{norm}(\mathbf{r}). \tag{198}$$

Its physical significance lies in the fact that it can be used to determine the maximum magnitude $E_{\max}$ of the induced electric field, defined as:

$$E_{\max} = \max_{\mathbf{r}\in\mathcal{B}} \left|\mathbf{E}(\mathbf{r})\right|. \tag{199}$$

$E_{\max}$ can be expressed in terms of the parameter $E_{\max}^{(inc)}$ of the incident field as follows:

$$E_{\max} = \omega K_E E_{\max}^{(inc)}. \tag{200}$$

Similarly, to characterize the heat generation due to dissipative power loss in a conductive medium, we introduce the coupling coefficient K_Q, defined as the maximum value of the normalized rate of heat generation within the conducting body:

$$K_Q = \max_{\mathbf{r}\in\mathcal{B}} Q_{norm}(\mathbf{r}). \tag{201}$$

K_Q has a significant physical role because it can be used to determine the maximum time-averaged rate of heat generation, $Q_{\max}$, defined as

$$Q_{\max} = \max_{\mathbf{r}\in\mathcal{B}} \left|Q(\mathbf{r})\right|. \tag{202}$$

$Q_{\max}$ can be expressed in terms of the parameter $E_{\max}^{(inc)}$ of the incident field as follows:

$$Q_{\max} = \omega^2 K_Q E_{\max}^{(inc)\,2}. \tag{203}$$

Notably, both K_E and K_Q are frequency-independent within the low-frequency approximation.

We apply the concepts defined earlier to study the following excitation scenarios. Scenario 0 involves a uniform incident electric field (110) oriented along the z-axis, whereas Scenarios 1 through 5 involve a point source at a distance h from the

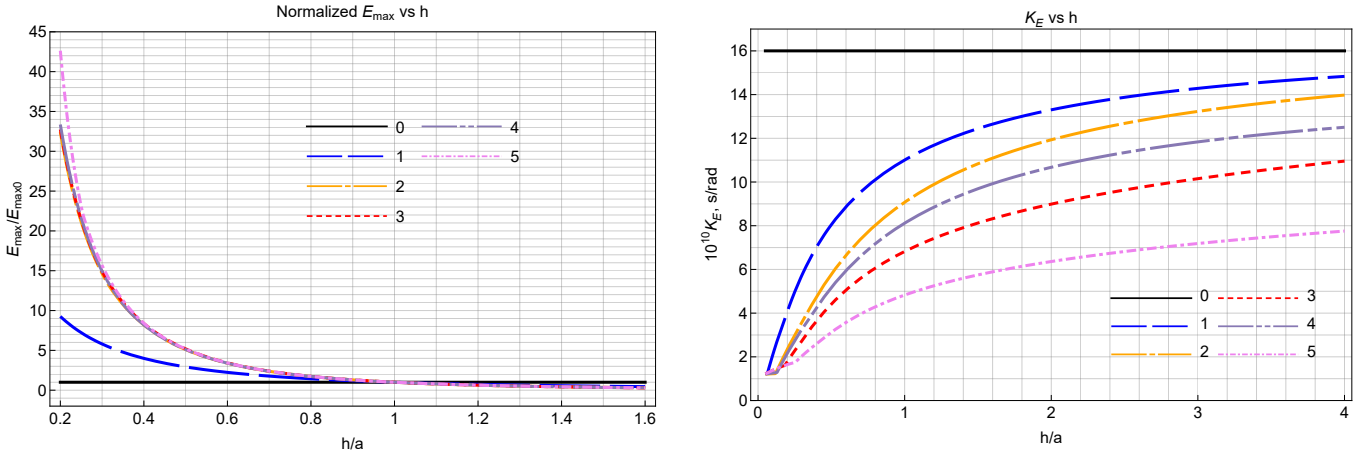

FIGURE 7. Dependence of the normalized $E_{\max}$ (defined as $E_{\max}(h)/E_{\max}(h_0)$, where $h_0 = a_0$) and the coupling coefficient K_E (defined in Eq. (198)) on the separation parameter h for Scenarios 0 through 5.

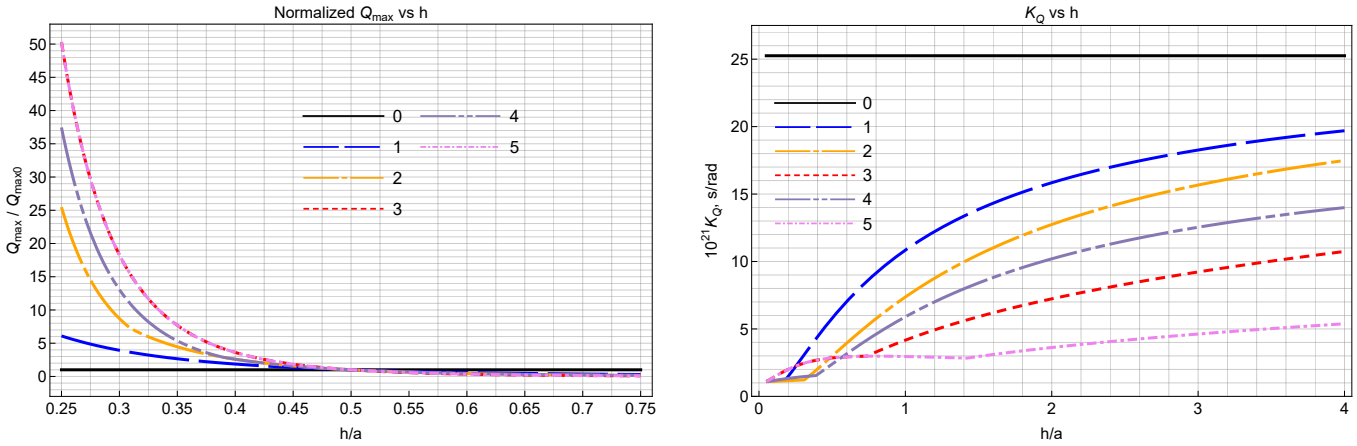

FIGURE 8. Dependence of the normalized $Q_{\max}$ (defined as $Q_{\max}(h)/Q_{\max}(h_0)$, where $h_0 = 0.5a_0$) and the coupling coefficient K_Q (defined in Eq. (201)) on the separation parameter h for Scenarios 0 through 5.

TABLE 2. Expressions for $E_{\max}^{(inc)}$ and the limit values of the coupling coefficients $K_E^{(\infty)}$ and $K_Q^{(\infty)}$ (in their respective units). For $h \to \infty$, the maximum on the right-hand side of Eqs. (198) and (201) occurs at the outer boundary $r = a_2$ of Layer 2.

Scenarios	0	1	2	3	4	5
$E_{\max}^{(inc)}$	$\lvert E_0\rvert$	$\frac{\lvert q\rvert}{4\pi\varepsilon_0 h^2}$	$\frac{\lvert p_z\rvert}{2\pi\varepsilon_0 h^3}$	$\frac{\lvert p_x\rvert}{4\pi\varepsilon_0 h^3}$	$\frac{\lvert p_z\rvert\sqrt{5}}{4\pi\varepsilon_0 h^3}$	$\frac{\lvert p_x\rvert\sqrt{2}}{4\pi\varepsilon_0 h^3}$
$10^9 K_E^{(\infty)}$	1.67976	1.6798	1.6798	1.6799	1.50281	1.18896
$10^{20} K_Q^{(\infty)}$	2.52533	2.52575	2.52575	2.52575	2.02129	1.26506

sphere. Specifically, Scenario 1 involves a point charge q, Scenario 2 — the dipole oriented along the z-axis: $\mathbf{p} = \mathbf{z}_0 p_z$, Scenario 3 — the dipole aligned with the x-axis: $\mathbf{p} = \mathbf{x}_0 p_x$, Scenario 4 — the circularly polarized[4] dipole with the polarization circle lying in the x-z plane: $\mathbf{p} = p_z(\mathbf{z}_0 + i\mathbf{x}_0)$, and Scenario 5 — the circularly polarized dipole with the polarization circle lying in the x-y plane: $\mathbf{p} = p_x(\mathbf{x}_0 + i\mathbf{y}_0)$.

To perform our computations, we needed the values of $E_{\max}^{(inc)}$ as defined in Eq. (191) for the scenarios mentioned. The explicit expressions for these values are summarized in Table 2. Although their derivations are straightforward, they are quite lengthy, so we omit them for brevity.

Figures 7 and 8 illustrate the dependence of $E_{\max}$, K_E (in Fig. 7), and $Q_{\max}$, K_Q (in Fig. 8), on the separation parameter h for the six excitation scenarios. For analysis, the dependencies $E_{\max}(h)$ and $Q_{\max}(h)$ are presented in normalized form using the ratios $E_{\max}/E_{\max\,0}$ and $Q_{\max}/Q_{\max\,0}$. Here, $E_{\max\,0}$ and

[4] According to the theory of time-harmonic vector fields [5, §§ 1.4.2, 1.4.3], [57, Sec. 7.4], the term 'polarization' describes the time evolution of the time-harmonic vector

$$\mathbf{P}(t) = \mathrm{Re}\, e^{-i\omega t}\mathbf{p}.$$

Here, we also use it to refer to the structure of the corresponding complex vector $\mathbf{p}$.

TABLE 3. Location of the maximum point $r_{\max}$ for the maximization problem (198) as a function of separation h. The separation is numerically characterized by the ratio h/a, which varies in increments of 0.005.

Location of $r_{\max}$	Scenarios					
	0	1	2	3	4	5
$r_{\max} = a_0$ Layer 1	n/a	0.05–0.06	0.05–0.115	0.05–0.18	0.05–0.125	0.05–0.25
$r_{\max} = a_1$ Layer 2	n/a	0.065–0.175	0.120–0.315	0.185–0.29	0.13–0.36	0.255–0.415
$r_{\max} = a_2$ Layer 2	∞	0.18–4.0	0.32–4.0	0.295–4.0	0.365–4.0	0.42–4.0

TABLE 4. Location of the maximum point $r_{\max}$ for the maximization problem (201) as a function of separation h. The separation is numerically characterized by the ratio h/a, which varies in increments of 0.005.

Location of $r_{\max}$	Scenarios					
	0	1	2	3	4	5
$r_{\max} = a_0$ Layer 1	n/a	0.05–0.18	0.05–0.305	0.05-0.73	0.05-0.385	0.05-1.42
$r_{\max} = a_1$ Layer 2	n/a	–	0.310–0.315	–	–	–
$r_{\max} = a_2$ Layer 2	∞	0.185–4.0	0.32–4.0	0.735–4.0	0.39–4.0	1.425–4.0

$Q_{\max 0}$ represent the values of $E_{\max}(h_0)$ and $Q_{\max}(h_0)$, where $h_0 = a_0$ for $E_{\max 0}$, and $h_0 = 0.5a_0$ for $Q_{\max 0}$. These ratios are frequency-independent.

The following insights are evident from these figures:

a) The coupling coefficients for the electric field (K_E) and generated heat (K_Q) are *higher* for a uniform incident field than for point sources. This suggests that using a uniform incident field can represent the *worst-case* exposure scenario involving a localized source.

b) The coupling coefficients K_E and K_Q for a point source *increase* with increasing distance h to the sphere, even as the induced field naturally *diminishes* with greater separation between the source and the sphere.

c) For localized sources such as a point charge, a linearly polarized dipole aligned with one of the Cartesian axes, or a circularly polarized dipole with a horizontal (x-y) plane of polarization, the coupling coefficients K_E and K_Q converge to those for the uniform incident field as $h \to \infty$.

This convergence is validated by calculating the limit values $K_E^{(\infty)}$ and $K_Q^{(\infty)}$, which represent K_E and K_Q as $h \to \infty$. The values of $K_E^{(\infty)}$ and $K_Q^{(\infty)}$, in units of $\mathrm{s\,rad^{-1}}$ and $\mathrm{m^{-1}\,s^2\,ohm^{-1}\,rad^{-2}}$, respectively, are presented in Table 2. For Scenarios 1 through 5, involving point sources, FD computations of the potentials $U, W_\perp, W_\parallel$ were carried out using the asymptotic forms (106)–(108), with h set to 1 m. Since the dependence of $E_{\max}^{(inc)}$ on h aligns with the corresponding asymptotic forms, we also used $h = 1$ m in the expressions for $E_{\max}^{(inc)}$ when calculating the coupling coefficients.

For Scenario 0 (uniform incident field), we used the explicit solution for the induced electric field derived from the potential $V_b(r,\theta) = i\omega\varepsilon_0 3E_0 v(r|1)\cos\theta$, which corresponds to the surface charge distribution in Eq. (109). The associated maximization problems (198) and (201) were solved analytically for θ, and numerically by simple search over a discrete set of values of r.

In our simulations involving point sources, we observed that the radial location $r_{\max}$ of the maximum magnitude of the induced electric field, as well as the maximum generated heat, is consistently found at a *structural boundary* within the conducting body. The maximum (or maxima, accounting for all values of ϕ, with $0 \le \phi \le 2\pi$, in ϕ-independent exposures due to a point charge or a z-oriented dipole) shifts from the outer boundary of the sphere ($r = a_0$) at small separations to the interfaces bounding layer 2 as separation increases. This shift is detailed in Tables 3 and 4, along with the radial location ($r = a_2$) of the maximum point for Scenario 0 (uniform incident field).

According to these Tables, the *piecewise-constant* functions $r_{\max}(h)$, corresponding to the respective maximization problems (198) or (201), can take one of three values: a_0, a_1, or a_2. These functions are defined by specifying intervals of constancy in the variable h. As shown in Tables 3 and 4, these intervals are *disjoint*, as the variable h has varied across a discrete set of 791 uniformly distributed values, starting at $h = 0.05a_0$, and ending at $h = 4a_0$, with a step of $0.005a$. Since the functions $E_{norm}(\mathbf{r})$ and $Q_{norm}(\mathbf{r})$ in Eqs. (198) and (201) are discontinuous across the interfaces, we also specify the *layer* from which

the point of maximum at an interface is approached. For convenience, the tables use the normalized variable h/a_0 instead of h.

Example of exposure assessment. Table 2 in [19] presents basic restrictions (BRs) for EM field exposure from 100 kHz to 300 GHz in terms of the specific energy absorption rate (SAR), averaged over a 10-g cubic mass of tissue and a time interval of at least 360 s. We shall denote the appropriately averaged SAR value for a given exposure as $\overline{R}$. Exposure levels respecting the established limits in [19] are defined by the condition:

$$\overline{R} < R_{BR}, \tag{204}$$

where R_{BR} is the BR value. The BRs for *local head* exposure in the frequency range from 100 kHz to 6 GHz, used in our analysis immediately below, are as follows [19, Tab. 2]: $R_{BR} = 2$ W/kg for general public exposure, and $R_{BR} = 10$ W/kg for occupational exposure.

Assuming that the exposure is due to a time-harmonic EM field, we have $\overline{R} \leq R_{\max}$, where $R_{\max}$ is the maximum value of the SAR, given by $R(\mathbf{r}) = Q(\mathbf{r})/m_d(\mathbf{r})$ [19, Eq. (10)]. In this expression, $Q(\mathbf{r})$ is the rate of heat generation defined in Eq. (196), and $m_d(\mathbf{r})$ is the mass density of the tissue at a given point. Based on this definition for $R(\mathbf{r})$, we can further derive:

$$\overline{R} \leq \frac{Q_{\max}}{m_{d,\min}}, \tag{205}$$

where $Q_{\max}$ is defined in Eq. (202), and $m_{d,min}$ is the minimum mass density within the given body part. To satisfy condition Eq. (204), it is *sufficient* to ensure $Q_{\max}/m_{d,min} < R_{BR}$. From this and Eq. (203) we obtain the following exposure condition on the parameter $E^{(inc)}_{\max}$:

$$E^{(inc)}_{\max} < \frac{1}{\omega}\sqrt{\frac{m_{d,\min}R_{BR}}{K_Q}}, \tag{206}$$

where K_Q is the coupling coefficient for a given exposure scenario.

Condition (206) is satisfied for *all* considered exposure scenarios if we: a) set K_Q to the highest value among those considered, as indicated in Table 2 for uniform field incidence, and b) set $m_{d,\min} = 1007\,\mathrm{kg/m^3}$, which is the mass density of CSF, the lowest among scalp, skull, CSF, and brain (as referenced in the IT'IS density database [17]).

Converting from angular frequency ω to cyclic frequency f_{MHz} (measured in MHz), and switching to the root mean square[5] (RMS) value, $E^{(inc)}_{\max,rms} = E^{(inc)}_{\max}/\sqrt{2}$, we obtain the following condition for the incident field in head exposures:

$$E^{(inc)}_{\max,rms} < \frac{1}{f_{\mathrm{MHz}}}\begin{cases}31781.6 & \text{(general public exposure)}\\ 71065.8 & \text{(occupational exposure)}\end{cases} \tag{207}$$

[5] In [19, Tab. 2], RMS values are used instead of the absolute values of complex amplitudes for time-harmonic quantities.

Note that all RMS electric field values in this paper are measured in units of V/m. At a frequency of 0.2 MHz, we have:

$$E^{(inc)}_{\max,rms} < \begin{cases}158,908\,\mathrm{V/m} & \text{(general public exposure)}\\ 355,329\,\mathrm{V/m} & \text{(occupational exposure)}\end{cases} \tag{208}$$

This can be compared with the limits defined by the reference levels in Table 6 of [19] for local exposure in the frequency range 0.1 MHz to 30 MHz:

$$E^{(inc)}_{\max,rms} < \frac{1}{f^{0.7}_{\mathrm{MHz}}}\begin{cases}671 & \text{(general public exposure)}\\ 1504 & \text{(occupational exposure)}\end{cases} \tag{209}$$

At 0.2 MHz, this leads to:

$$E^{(inc)}_{\max,rms} < \begin{cases}2070.15\,\mathrm{V/m} & \text{(general public exposure)}\\ 4640.09\,\mathrm{V/m} & \text{(occupational exposure)}\end{cases} \tag{210}$$

We can see that the low-frequency electric field levels specified in Eq. (208) are significantly *higher* than those in Eq. (210). (Mathematically, the terms on the right-hand side of Eq. (207) are larger than those on the right-hand side of Eq. (209) for all frequencies up to approximately 384.4 GHz for general public exposure and 381.3 GHz for occupational exposure).

As a final example, let us consider Table 4 in [19] which specifies BRs for EM exposure of any body part in the frequency range of 100 kHz to 10 MHz, based on peak spatial values. These restrictions are defined in terms of spatially averaged RMS values of the induced electric field, over a 2 mm × 2 mm × 2 mm volume of contiguous tissue. We denote these RMS values by $\overline{E}_{rms}$. Exposure levels respecting these restrictions are defined by the condition:

$$\overline{E}_{rms} < E_{BR,rms}, \tag{211}$$

where $E_{BR,rms}$ represents the BRs established in [19, Tab. 4], measured in V/m: $E_{BR} = 1.35 \cdot 10^{-4} f_{\mathrm{Hz}}$ for general public exposure, and $E_{BR,rms} = 2.7 \cdot 10^{-4} f_{\mathrm{Hz}}$ for occupational exposure, with f_{Hz} being the frequency in Hz.

For a time-harmonic field, it is clear that

$$\overline{E}_{rms} < E_{\max,rms}, \tag{212}$$

where $E_{\max,rms} = E_{\max}/\sqrt{2}$. To satisfy condition (211), it is *sufficient* to ensure that $E_{\max,rms} < E_{BR,rms}$. From this and Eq. (200), we can derive the following exposure condition for the parameter $E^{(inc)}_{\max,rms}$:

$$E^{(inc)}_{\max,rms} < \frac{1}{\omega}\frac{E_{BR,rms}}{K_E}, \tag{213}$$

where K_E is the field coupling coefficient for a given exposure scenario.

Condition (213) is met for *all* analyzed exposure scenarios if K_E is set to the highest value provided in Table 2, which corresponds to uniform field incidence. Converting from angular frequency ω to cyclic frequency f_{Hz}, we obtain the following condition for the incident field:

$$E^{(inc)}_{\max,rms} < \begin{cases}12,791.1\,\mathrm{V/m} & \text{(general public exposure)}\\ 25,582.1\,\mathrm{V/m} & \text{(occupational exposure)}\end{cases} \tag{214}$$

This can be compared with the limits defined by the reference levels in Table 8 of [19] for local exposure in the frequency range 100 kHz to 10 MHz:

$$E_{\max,rms}^{(inc)} < \begin{cases} 83\,\text{V/m} & \text{(general public exposure)} \\ 170\,\text{V/m} & \text{(occupational exposure)} \end{cases} \quad (215)$$

Thus, we can see that the low-frequency electric field limits specified in Eq. (214) are significantly *higher* than those in Eq. (215).

Our estimates suggest that the existing reference levels for the electric field, as specified in [19, Tabs. 6, 8], are *conservative* when the incident EM field is low-frequency and predominantly electric [14, Sec. 6.5]. This scenario is typical of emerging WPT technologies [9, 13, 63] that employ capacitive coupling.

However, these exposure assessments should *not* be taken as guidance for practical applications. Validation through further research is essential due to various limitations. Notably, our assumption of a *spherical* stratification model for the head may necessitate additional anatomical detail. Moreover, we did not consider the influence of *nearby* dielectric and conducting objects, which can affect low-frequency electric fields. Furthermore, our model did not incorporate the impact of the entire *human body* on the induced electric field within the head. While suitable for highly localized exposures, this assumption may be inadequate as the interaction area expands, potentially leading to conduction currents flowing into *other* body parts or to the ground.

ACKNOWLEDGEMENT

Mykola Bogomolov's research was partially supported by the Council for At-Risk Academics (CARA). Greg Gajda and Mykola Zhuk express their gratitude to Michelle O'Brien and Jason Zawalek for their motivation and encouragement throughout the development of this work. The authors also extend their sincere thanks to Abdel Alzahed, Narine Martel, and Alp Ozgun, as well as to the anonymous reviewers of this paper, for their valuable and constructive feedback during the review process.

REFERENCES

[1] Ames, W. F., *Numerical Methods for Partial Differential Equations*, 2nd ed., Academic Press, New York, NY, 1977.

[2] Athanasiadis, C., "Low-frequency electromagnetic scattering theory for a multi-layered scatterer," *The Quarterly Journal of Mechanics and Applied Mathematics*, Vol. 44, No. 1, 55–67, Feb. 1991.

[3] Batygin, V. V. and I. N. Toptygin, *Problems in Electrodynamics*, 2nd ed., Academic Press, London, UK, 1978.

[4] Berdichevsky, M. N. and V. I. Dmitriev, *Magnetotellurics in the Context of the Theory of Ill-Posed Problems*, Society of Exploration Geophysicists, 2002.

[5] Born, M. and E. Wolf, *Principles of Optics*, 7th ed., Cambridge University Press, Cambridge, UK, 1999.

[6] Chew, H., P. J. McNulty, and M. Kerker, "Model for Raman and fluorescent scattering by molecules embedded in small particles," *Physical Review A*, Vol. 13, No. 1, 396–404, Jan. 1976.

[7] Chew, H., M. Kerker, and P. J. McNulty, "Raman and fluorescent scattering by molecules embedded in concentric spheres," *Journal of the Optical Society of America*, Vol. 66, No. 5, 440–444, May 1976.

[8] Chew, H., M. Kerker, and D. D. Cooke, "Electromagnetic scattering by a dielectric sphere in a diverging radiation field," *Physical Review A*, Vol. 16, No. 1, 320–323, Jul. 1977.

[9] Dai, J. and D. C. Ludois, "A survey of wireless power transfer and a critical comparison of inductive and capacitive coupling for small gap applications," *IEEE Transactions on Power Electronics*, Vol. 30, No. 11, 6017–6029, Nov. 2015.

[10] Dassios, G. and A. S. Fokas, *Electroencephalography and Magnetoencephalography: An Analytical-Numerical Approach*, De Gruyter, Berlin, Germany, 2020.

[11] Dassios, G. and R. Kleinman, *Low Frequency Scattering*, Clarendon Press, Oxford, UK, 2000.

[12] Durney, C. H., H. Massoudi, and M. F. Iskander, *Radiofrequency Radiation Dosimetry Handbook*, 4th ed., USAF School of Aerospace Medicine, Brooks AFB, Brooks, TX, 1986.

[13] Erfani, R., F. Marefat, A. M. Sodagar, and P. Mohseni, "Modeling and experimental validation of a capacitive link for wireless power transfer to biomedical implants," *IEEE Transactions on Circuits and Systems II: Express Briefs*, Vol. 65, No. 7, 923–927, Jul. 2018.

[14] Fano, R. M., L. J. Chu, and R. B. Adler, *Electromagnetic Fields, Energy, and Forces*, John Wiley & Sons, New York, NY, 1960.

[15] Gao, Y., Q.-Y. Di, R. Wang, C.-M. Fu, P.-F. Liang, and F.-H. Zheng, "Strength of the electric dipole source field in multilayer spherical media," *IEEE Transactions on Geoscience and Remote Sensing*, Vol. 60, 5902612, 2021.

[16] Gavrilyuk, I., M. Hermann, V. Makarov, and M. V. Kutniv, *Exact and Truncated Difference Schemes for Boundary Value ODEs*, Springer Science & Business Media, 2011.

[17] Hasgall, P. A., F. D. Gennaro, C. Baumgartner, E. Neufeld, B. Lloyd, M. C. Gosselin, D. Payne, A. Klingenbock, and N. Kuster, "IT'IS Database for thermal and electromagnetic parameters of biological tissues, version 4.1," IT'IS Foundation, Zurich, Switzerland, Feb. 2022.

[18] Hulst, Van de H. C., *Light Scattering by Small Particles*, John Wiley & Sons, New York, NY, 1957.

[19] ICNIRP (International Commission on Non-Ionizing Radiation Protection), "Guidelines for limiting exposure to electromagnetic fields (100 kHz to 300 GHz)," *Health Physics*, Vol. 118, No. 5, 483–524, May 2020.

[20] Imura, T., *Wireless Power Transfer Using Magnetic and Electric Resonance Coupling Techniques*, Springer Singapore, Singapore, 2020.

[21] Jackson, J. D., *Classical Electrodynamics*, 3rd ed., John Wiley & Sons, Hoboken, NJ, 1999.

[22] Kai, L. and P. Massoli, "Scattering of electromagnetic-plane waves by radially inhomogeneous spheres: A finely stratified sphere model," *Applied Optics*, Vol. 33, No. 3, 501–511, Jan. 1994.

[23] Kalogeropoulos, A. and N. L. Tsitsas, "Analytical algorithms for direct and inverse problems pertaining to the electromagnetic excitation of a layered medium by N dipoles," *Mathematical Methods in the Applied Sciences*, Vol. 46, No. 16, 16 734–16 760, Nov. 2023.

[24] Kleinman, R. E., "Low frequency solution of electromagnetic scattering problems," *Electromagnetic Wave Theory*, 891–905, Pergamon Press, 1967.

[25] Lekner, J., *Electrostatics of Conducting Cylinders and Spheres*, AIP Publishing, 2021.

[26] LeVeque, R. J., *Finite Difference Methods for Ordinary and Partial Differential Equations: Steady-State and Time-Dependent Problems*, SIAM, 2007.

[27] Li, L.-W., P.-S. Kooi, M.-S. Leong, and T.-S. Yee, "Electromagnetic dyadic Green's function in spherically multilayered media," *IEEE Transactions on Microwave Theory and Techniques*, Vol. 42, No. 12, 2302–2310, Dec. 1994.

[28] Lin, J. C., *Electromagnetic Fields in Biological Systems*, CRC Press, 2012.

[29] Mackay, T. G. and A. Lakhtakia, *Modern Analytical Electromagnetic Homogenization with Mathematica*, 2nd ed., IOP Publishing, 2020.

[30] March, H. W., "The field of a magnetic dipole in the presence of a conducting sphere," *Geophysics*, Vol. 18, No. 3, 671–684, Jul. 1953.

[31] Moroz, A., "A recursive transfer-matrix solution for a dipole radiating inside and outside a stratified sphere," *Annals of Physics*, Vol. 315, No. 2, 352–418, Feb. 2005.

[32] De Munck, J. C., "The potential distribution in a layered anisotropic spheroidal volume conductor," *Journal of Applied Physics*, Vol. 64, No. 2, 464–470, Jul. 1988.

[33] Naess, S., C. Chintaluri, T. V. Ness, A. M. Dale, G. T. Einevoll, and D. K. Wójcik, "Corrected four-sphere head model for EEG signals," *Frontiers in Human Neuroscience*, Vol. 11, 490, Oct. 2017.

[34] Nieminen, J. O. and M. Stenroos, "The magnetic field inside a layered anisotropic spherical conductor due to internal sources," *Journal of Applied Physics*, Vol. 119, No. 2, 023901, Jan. 2016.

[35] Nunez, P. L. and R. Srinivasan, *Electric Fields of The Brain: The Neurophysics of EEG*, 2nd ed., Oxford University Press, 2006.

[36] Osipov, A. V. and S. A. Tretyakov, *Modern Electromagnetic Scattering Theory with Applications*, John Wiley & Sons, 2017.

[37] Papargiri, A., V. S. Kalantonis, D. Kaziki, P. Vafeas, and G. Fragoyiannis, "Revisiting an analytical solution for the three-shell spherical human head model in electroencephalography," *Partial Differential Equations in Applied Mathematics*, Vol. 4, 100178, Dec. 2021.

[38] Perelman, A. Y., "Scattering by particles with radially variable refractive indices," *Applied Optics*, Vol. 35, No. 27, 5452–5460, 1996.

[39] Petrov, Y., "Anisotropic spherical head model and its application to imaging electric activity of the brain," *Physical Review E*, Vol. 86, No. 1, 011917, Jul. 2012.

[40] Prokopiou, P. and N. L. Tsitsas, "Electromagnetic excitation of a spherical medium by an arbitrary dipole and related inverse problems," *Studies in Applied Mathematics*, Vol. 140, No. 4, 438–464, May 2018.

[41] Rasskazov, I. L., P. S. Carney, and A. Moroz, "STRATIFY: A comprehensive and versatile MATLAB code for a multilayered sphere," *OSA Continuum*, Vol. 3, No. 8, 2290–2306, 2020.

[42] Reyhani, S. M. S. and R. J. Glover, "Electromagnetic dyadic Green's function for a multilayered homogeneous lossy dielectric spherical head model for numerical EMC investigation," *Electromagnetics*, Vol. 20, No. 2, 141–153, 2000.

[43] Samarskii, A. A. and I. V. Fryazinov, "On the convergence of difference schemes for a heat-conduction equation with discontinuous coefficients," *USSR Computational Mathematics and Mathematical Physics*, Vol. 1, No. 4, 962–982, 1962.

[44] Samarskii, A. A., *The Theory of Difference Schemes*, Marcel Dekker, 2001.

[45] Santos, F. C. and A. C. Tort, "The electrostatic field of a point charge and an electrical dipole in the presence of a conducting sphere," *European Journal of Physics*, Vol. 25, No. 6, 859–868, Nov. 2004.

[46] Shalaev, V. M., "Electromagnetic properties of small-particle composites," *Physics Reports*, Vol. 272, No. 2-3, 61–137, Jul. 1996.

[47] Sihvola, A. H., *Electromagnetic Mixing Formulas and Applications*, Institution of Engineering and Technology, IEE, London, UK, 2008.

[48] Smythe, W. R., *Static and Dynamic Electricity*, 3rd ed., Hemisphere Publishing Corporation, New York, NY, 1989.

[49] Stakgold, I. and M. Holst, *Green's Functions and Boundary Value Problems*, 3rd ed., John Wiley & Sons, 2011.

[50] Staebler, P., *Human Exposure to Electromagnetic Fields: From Extremely Low Frequency (ELF) to Radiofrequency*, John Wiley & Sons, 2017.

[51] Stevenson, A. F., "Solution of electromagnetic scattering problems as power series in the ratio (dimension of scatterer)/wavelength," *Journal of Applied Physics*, Vol. 24, No. 9, 1134–1142, Sep. 1953.

[52] Stefanidou, E., P. Vafeas, and F. Kariotou, "An analytical method of electromagnetic wave scattering by a highly conductive sphere in a lossless medium with low-frequency dipolar excitation," *Mathematics*, Vol. 9, No. 24, 3290, 2021.

[53] Stratton, J. D., *Electromagnetic Theory*, McGraw-Hill, 1941.

[54] Sumner, J. S., *Principles of Induced Polarization for Geophysical Exploration*, Elsevier, 2012.

[55] Tai, C.-T., *Dyadic Green Functions in Electromagnetic Theory*, 2nd ed., IEEE Press, 1994.

[56] Tikhonov, A. N. and A. A. Samarskii, "Homogeneous difference schemes of a high degree of accuracy on non-uniform nets," *USSR Computational Mathematics and Mathematical Physics*, Vol. 1, No. 3, 465–486, 1962.

[57] Van Bladel, J. G., *Electromagnetic Fields*, 2nd ed., John Wiley & Sons, 2007.

[58] Vafeas, P., G. Perrusson, and D. Lesselier, "Low-frequency solution for a perfectly conducting sphere in a conductive medium with dipolar excitation," *Progress In Electromagnetics Research*, Vol. 49, 87–111, 2004.

[59] Wait, J. R., "On the electromagnetic response of a conducting sphere to a dipole field," *Geophysics*, Vol. 25, No. 3, 649–658, Jun. 1960.

[60] Wait, J. R. and K. P. Spies, "Electromagnetic induction in a conducting sphere with a concentric shell," *Radio Science*, Vol. 4, No. 6, 557–560, Jun. 1969.

[61] Wait, J. R., "Electromagnetic induction in a solid conducting sphere enclosed by a thin conducting spherical shell," *Geophysics*, Vol. 34, No. 5, 753–759, Oct. 1969.

[62] Wait, J. R., *Geo-Electromagnetism*, Academic Press, 1982.

[63] Wang, Z., Y. Zhang, X. He, B. Luo, and R. Mai, "Research and application of capacitive power transfer system: A review," *Electronics*, Vol. 11, No. 7, 1158, 2022.

[64] Ward, S. H. and G. W. Hohmann, "Electromagnetic theory for geophysical applications," *Electromagnetic Methods in Applied Geophysics — Theory*, Vol. 1, 130–311, SEG, 1987.

[65] Wriedt, T., "Mie theory: A review," *The Mie Theory: Basics and Applications*, 53–71, Springer, 2012.

[66] Yeh, C., "Dyadic Green's function for a radially inhomogeneous spherical medium," *Physical Review*, Vol. 131, No. 5, 2350–2353, Sep. 1963.